2023

Structural Transformations in Photo-Thermo-Refractive Glass for Hologram Recording

Roberto Alejandro Alvarez Aguirre
University of Central Florida

STRUCTURAL TRANSFORMATIONS IN PHOTO-THERMO-REFRACTIVE GLASS FOR HOLOGRAM RECORDING

by

ROBERTO ALVAREZ

B.S. Autonomous University of Nuevo Leon UANL, 2013
M.S. University of Central Florida, 2019

A dissertation submitted in partial fulfillment of the requirements
for the degree of Doctor of Philosophy
in CREOL, The College of Optics and Photonics
at the University of Central Florida
Orlando, Florida

Spring Term
2023

Major Professor: Leonid Glebov

ABSTRACT

This dissertation focuses on the structural transformations in photo-thermo-refractive (PTR) glass that enable recording phase holograms for efficient transformation of optical beams and high resolution spectroscopy. PTR glass is a multicomponent silicate matrix doped with Ce, Ag, Sn and Sb. It is a holographic phase medium with the ability of permanent refractive index change after UV exposure and thermal development above 500°C due to the precipitation of a NaF crystalline phase. Electronic processes are studied by analyzing the structure of absorption and luminescence bands of PTR glass matrix and its dopants.

We analyze the structural transformations in PTR glass from the perspective of induced optical scattering. A high-sensitivity experimental setup for measuring scattering at 90° with respect to a 1-mm diameter probe beam at 405 nm was constructed. A specific algorithm of UV exposures and thermal regimes to reveal the lowest temperature at which inhomogeneities arise was proposed. It was shown that no scattering increase observed in UV exposed PTR glass after thermal processing at temperatures below 450°C. This means that all structural transformations produced by this treatment occurred at atomic scale.

Finally, we discuss the low temperature ion exchange method. We describe the theoretical basis of this method and present an experimental layout capable of performing low-temperature ion exchange in the surface of PTR samples. Results of a system that provides measurements of surface refractive index called ‘the waveguide method’ is presented. It is shown how this system can be used for the characterization of planar optical waveguides created on the surface of PTR glass samples and how their refractive index profile can be calculated by the inverse Wentzel-Kramers-Brillouin (WKB) method.

ACKNOWLEDGMENTS

I would like to acknowledge my PhD advisors Dr. Leonid Glebov, Dr. Ivan Divliansky, Dr. Kathleen Richardson, Dr. Talat Rahman and Dr. Pavel Shirshnev who guided me to conduct the research presented in this dissertation. I want to thank them for their fruitful comments, academic support and motivation. Specially, I would like to acknowledge all my laboratory colleagues from PPL group at CREOL and OptiGrate who helped me every day to obtain the results shown herein. I am also very thankful for my parents and family members for their emotional support throughout my endeavor. I enormously thank the government of Mexico and its National Council of Science and Technology (CONACYT) for partial funding of my PhD studies.

TABLE OF CONTENTS

LIST OF FIGURES

LIST OF TABLES

CHAPTER 1: INTRODUCTION TO PTR GLASS SCIENCE AND ITS REFRACTIVE INDEX CHANGE MECHANISM

1.1 Motivation and Objective

PTR glass has been widely studied on recent years due to its exceptional capabilities as a holographic phase medium. This is thanks to the ability of achieving a permanent refractive index change after exposure in the photosensitive band of the material (280 nm – 350 nm) and subsequent thermal development above 500 °C. Therefore, our main motivation is the investigations of the nature of optical characteristics of glass as a material for laser industry. A variety of holographic optical elements recorded in the bulk of this material such as beam splitters, mirrors and lenses can be found in multiple applications including imaging, wavefront shaping and laser beam control. Impressively, such structures can withstand temperatures up to 400 °C without significant deterioration of its holographic efficiency properties. More important advantages of PTR glass with respect to other holographic materials are its maximum attainable refractive index change (RIC) (up to 1000 ppm) and the ability of high resolution, which allows recording structures with spatial frequencies as high as 10,000 lines per mm. Moreover, PTR glass exhibits a window of complete optical transparency (low absorption) that ranges from 350 nm – 2700 nm. This feature grants an exceptional tolerance to optical radiation, with laser damage thresholds of 40 kW/cm^2 for CW sources and 40 J/cm^2 for 10 ns pulsed laser beams. On the other hand, the linear glass thermal variations of the refractive index (dn/dt) are very low, its thermo-optic coefficient falls below 5×10^{-6} / °K, which allows classifying the glass almost as an athermal material. At the same time, the PTR glass has all advantages of high-quality laser optics glass: ultralow scattering and ultralow absorption in

operational spectral range, the optical homogeneity required for holography, low-nonlinear refractive index and low coefficient of thermal expansion.

However, despite the demonstration of efficient holographic optical elements produced by the photo-thermo-refractive process and its development to commercial stage, the main origin of its refractive index change mechanism and specific conditions of structural transformations of vitreous and crystalline phases remains unclear. Many puzzles about PTR glass functioning nature are still unsolved: What is the real refractive index change mechanism of PTR glass? What is the role of bromine and water concentration in the photo-induced crystallization properties of the material? Could the laser damage threshold of PTR glass be improved? At which temperature in the photo-thermo-refractive process do structural inhomogeneities start to appear? What is the lowest available level of scattering in PTR glass?

For this reason, the main objective of this work is to provide insightful information on the structural transformations involved at each stage of the photo-thermo-refractive process necessary for hologram recording. The goal is to propose possible conditions for separation of optically and thermally induced phenomena as an attempt to breakdown the complete refractive index change mechanism.

1.2 Background

The first photosensitive glass for photography based on crystalline phase precipitation was discovered by Dr. Donald Stookey in 1949 at Corning NY [1]. It was initially proposed as a new type of photographic medium based on a silicate glass matrix with an addition of metallic constituents (photosensitive ingredients) capable of producing a 3D image after exposure to actinic radiation followed by thermal treatment. Stookey developed two basic types of glasses: color transparencies (1) and photosensitive opal (2). In color transparencies, the image was

produced by submicron particles of photosensitive metals like Cu, Au or Ag. Whereas photosensitive opal consisted in the formation of particles of Ag or Au within the glass that served as nuclei for the growth of different types of microscopic crystals in the thermal development stage [1]. The photosensitive additions employed were classified as photosensitive metals (Au, Cu or Ag), thermo-reducing agents (mainly compounds of Sn and Sb) and optical sensitizers. Optical sensitizers are distinguished by a photosensitivity spectrum of a material being shifted to new optical wavelengths corresponding to absorption bands of the sensitizer. For example, this particular glass contained the Ce^{3+} ion as an optical sensitizer that absorbed light to produce a photochemical reaction of gold activated by cerium [1].

$$Ce^{3+} + Au^{+} + hv \rightarrow Ce^{4+} + Au^{0} \quad (1\text{-}1)$$

With a wide variety of glass compositions and physical properties, the capability of recording structures in many colors, intensities and depth of penetrations was demonstrated. However, despite the discovery of this new type of photosensitive medium and its development to commercial stage, absorption and strong scattering produced by metallic clusters and precipitation of crystals did not let it to hold up as the attractive photographic material of the market.

After discovery of holography [3], efforts for finding an efficient volume holographic medium continued mainly with organic compounds, until late 1980s when stable photo-induced RIC was demonstrated in inorganic glass and relatively highly efficient holographic elements were demonstrated [2]. One of the unique characteristics of holography in comparison to photography is the ability to incorporate phase and not only amplitude into the holographic element [3]. Hence, the following efforts exploring holographic phase media from 1990s were performed with Na-Zn-Al silicate glasses doped with fluorine, boron, silver, cerium, antimony

and tin [4]. In recent years, PTR glass has become the preferred optical material for holographic recording needed in high power laser applications. It demonstrates low absorption for a large number of wavelengths and highly efficient performance of diffractive optical elements [5]. Nowadays, holographic optical elements recorded in PTR glass encounter many applications in several fields including data storage and processing, fine filtering of laser radiation and beam combining for high power laser systems. Nevertheless, new photosensitive media are still in development [6] exploring new compositions and technological conditions in order to expand the glass capabilities and potential applications.

1.3 A new volume photosensitive media for hologram recording

It was until 1990s when PTR glass was significantly improved by Dr. Leonid Glebov and co-workers at CREOL, University of Central Florida, USA [7]. This type of glass is a multicomponent silicate matrix doped with minor amounts of cations Ag, Ce, Sb and Sn and anions F and Br. Since its development became very successful in the holography industry after proving high optical homogeneity, high transparency for a wide range of wavelengths and high tolerance to temperature and optical radiation. Recent improvements of PTR glass resulted in the demonstration of highly efficient volume Bragg gratings (VBGs) that exceed 99.99% relative diffraction efficiency and very low losses. Moreover, holographic elements fabricated in PTR glass have proved to be excellent for applications like narrowband spectral and angular filtering, spectral locking of laser radiation, high power laser beam combining, and mode selection in volume Bragg lasers.

1.4 Applications, general properties and examples of holographic optical elements recorded in PTR glass

Current PTR glass technology is capable to fabricate volume gratings with spatial frequencies that range from 50 /mm up to 10,000 /mm. It has been demonstrated that reflecting (RBG) and transmitting (TBG) Bragg gratings can achieve an absolute diffraction efficiency of 95 % and relative diffraction efficiency of 99.9 %. Spectral selectivity is one of the main attributes of VBGs [8]. For example, ultra-narrow spectral selectivity properties can be achieved for RBGs going down to 10 pm spectral width acceptance. This property can be extremely useful especially when filtering laser light sources. A standard spectral selectivity curve contains a maximum (Gaussian-like envelope) with two side lobes separated by zeroes. Therefore, if a beam is deviated from the Bragg condition (the maximum in spectral selectivity curve) it will not experience diffraction at all and will be just transmitted. This property of VBGs combined to their high resistance to optical radiation was a key feature for the demonstration of high power beam combining in [9]. In such experiments, a total output power of 755 W was accomplished by the combination of five high power laser beams and by using the property of thermal tuning of the resonant wavelength. This is possible because PTR glass experiences a thermal shift of the Bragg wavelength of about 7 pm/ °K in the NIR spectral region.

As previously mentioned, one of the main advantages of VBGs in comparison with the rest of the holographic materials of the market is their high temperature stability and optical radiation tolerance. In contrast with materials like doped lithium niobate the holographic element will not be damaged when working under a high-power optical beam. The laser damage threshold of PTR glass reaches 40 kW/cm^2 for CW sources and 40 J/cm^2 for 10 ns pulsed laser beams. Unlike photopolymers and photoresists, in PTR glass the heating of the

element will not break down the recorded hologram. Experimental demonstrations showed [10] that the diffraction efficiency performance of the gratings will be stable even when the gratings reached a temperature of 400 °C. In addition, another advantage would be the possibility of recording several structures on the same holographic element (multiplexed gratings). This can be accomplished by sequential UV exposures in the recording process since in general no induced RIC is obtained until the thermal treatment stage reaches above 485 °C. So, if one attempts to create these multiplexed elements it will be only limited by the intrinsic capacity of attaining a maximum refractive index change in the glass (photosensitivity). In the works of [11] it was demonstrated the recording of a 5-TBG multiplexed hologram in a 5-mm glass sample, achieving a total diffraction efficiency above 99.9%. More examples of holographic optical elements recorded in the volume of PTR glass includes longitudinal and transverse chirped gratings, apodized gratings, volume phase masks and holographic phase masks [12].

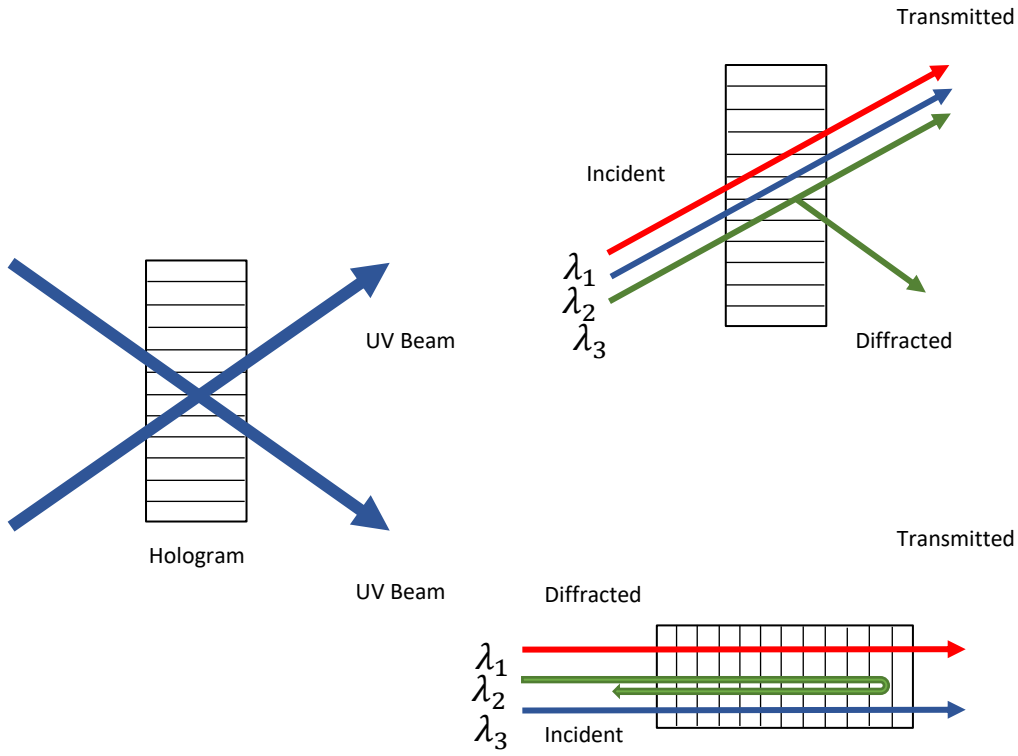

Figure 1-1 Optical scheme for the recording of VBG by interference pattern of two coherent collimated UV beams (left). Transmitting (top, right) and reflecting (bottom, right) VBG configurations

1.5 PTR glass fabrication process

The general procedure for PTR glass fabrication is the following [13].

(1) Batch Preparation: The chemical compounds are weighed separately and mixed in a composition (mol %) of 15 Na_2O – 4 Al_2O_3 – 70 SiO_2 – 5 NaF – 5 ZnO – 1 KBr, with minor amounts of dopants Ce, Ag, Sb and Sn of about ~ 0.01. To ensure homogenization of the batch, mechanical mixing is applied for 1 hour.

(2) Melting: The batch originally loaded as a homogeneous mixture of chemical powders is heated up to 1460 °C in a platinum crucible for few hours in a high-temperature melting furnace. To prevent technological contamination of the batch from external agents (like metals, synthetic fabrics or any other type of impurities) guidelines of the operational procedure should be followed with extreme caution.

(3) Homogenization: Mechanical platinum stirrer is needed during the melting process to ensure chemical homogeneity.

(4) Cooling: Fast cooling of PTR glass melt to temperatures below 500 °C is critical to avoid spontaneous crystallization.

(5) Annealing: The glass undergoes an isothermal aging for two hours at 460 °C then subsequently ramps down at a cooling rate of about 0.1 °C/min. A full annealing cycle usually extends from 24 to 48 hours.

Figure 1-2 High-temperature glass melting furnaces installed in the glass laboratory at CREOL

1.6 Fundamental physical and chemical properties of PTR glass

PTR glass is a crown-type optical glass with Abbe number $\nu_d = 59.2$ and a density value of $\rho = 2504$ Kg/m^3 [14]. The optical spectrum of this glass includes a window of complete transparency that ranges from 350 nm to 2700 nm and an index of refraction of 1.4959 at 587.5 nm. As one of the main optical materials used in holography and high power laser applications, the nonlinear properties of the material are of main relevance [14]. Investigations of this glass studied under femtosecond radiation revealed that the nonlinear refractive index of PTR glass is $n_2 = 3.3 \times 10^{-20}$ m^2/W, which is very close to the value measured for fused silica [15]. Moreover, the nonlinear refractive index of PTR does not seem to change after UV exposure and thermal treatment. The absorption spectrum of virgin (meaning unexposed and not thermally developed) PTR glass in a range of 250 nm to 3200 nm is presented in Fig. 1.3.

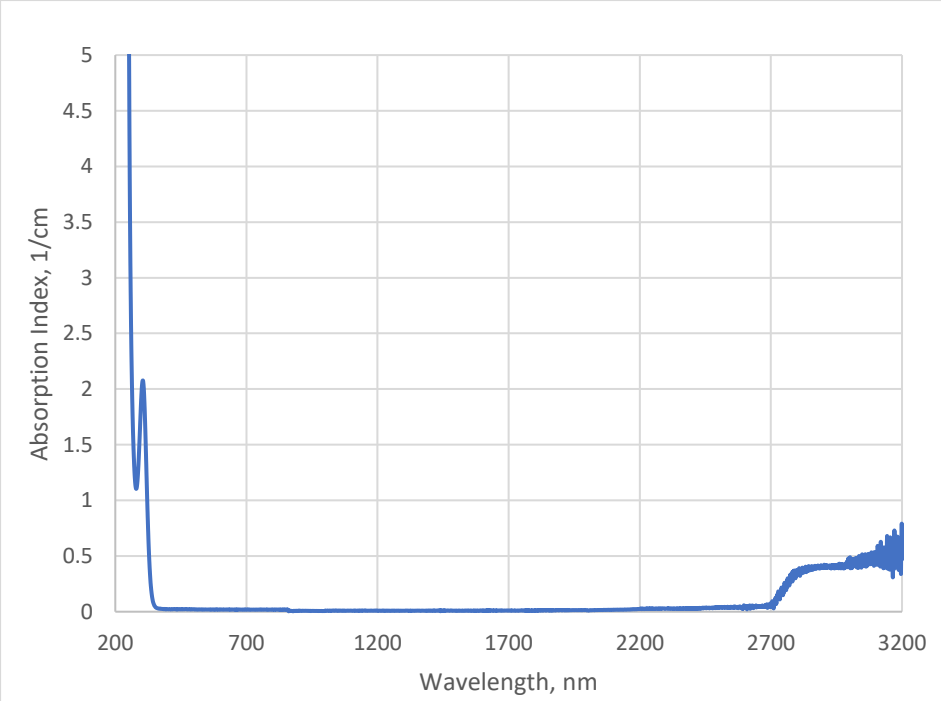

Figure 1-3 Absorption spectrum of pristine PTR glass

Here we can see the Near Infrared (NIR) absorption edge of PTR glass around 2.9 μm, which is mainly conformed by the absorption of hydroxyl (OH^-) groups. Such radicals are formed during the glass melting process when chemical transformations start to occur at temperatures beyond 300 °C. In Figure 1.4, we can observe plots of the IR edge of PTR glass exhibiting different levels of dehydration. This is achievable through technological modifications of the glass melting fabrication process. At high levels of dehydration, this part of spectrum is the mix of hydroxyl absorption bands and multiphonon absorption of glass matrix.

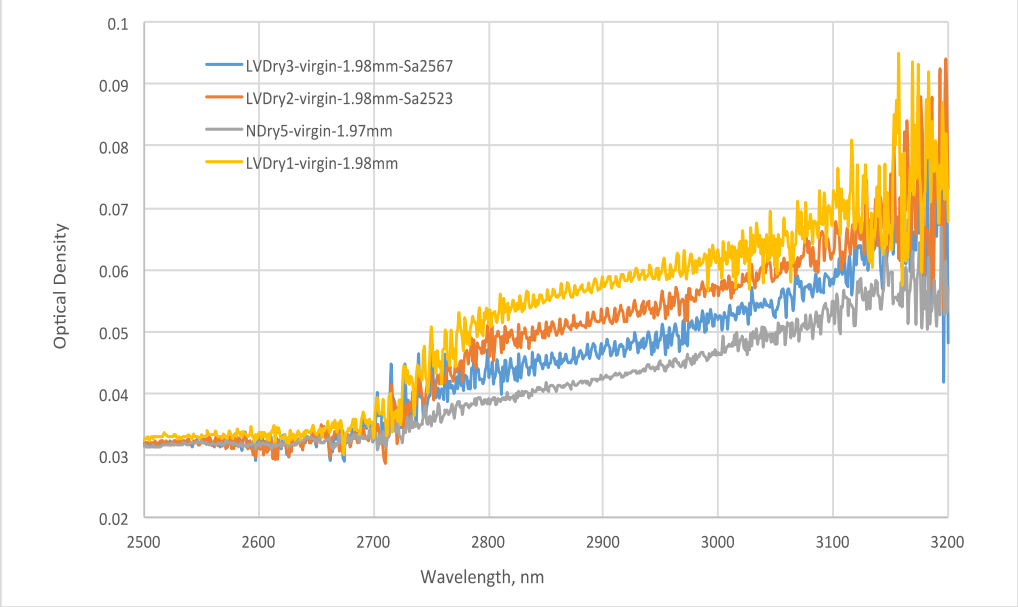

Figure 1-4 NIR absorption spectra of dehydrated pristine PTR glasses

The UV absorption edge of the material at virgin stage includes a trivalent cerium band with maximum at 305 nm and additional bands associated with Ce^{4+} , Sb^{3+}, and Ag^{+} that contribute to the short wavelength absorption edge (Fig. 1.5). Intrinsic absorption of glass matrix with maximum in vacuum UV region nm that can be modeled with an exponential function [16] could be observed in pure PTR glass matrix at wavelengths shorter 210 nm. In regular PTR glasses, Ce^{3+} ion serves as the optical sensitizer and hence its absorption properties determine the photosensitivity band of the material. In this case, such band ranges from 280 to 350 nm. Therefore, all photo-induced processes of regular PTR glass are triggered by exposure to near UV light with photon energies of 3.10 – 4.13 eV.

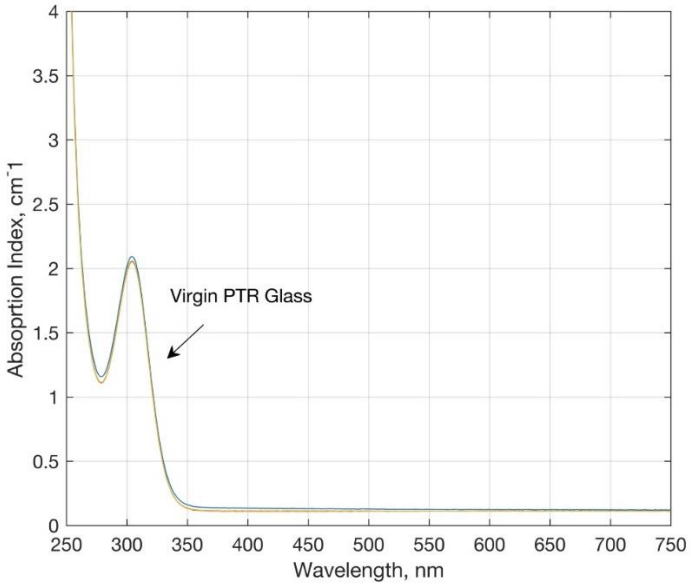

Figure 1-5 UV and visible absorption spectra of pristine PTR glass

As it was mentioned before, the chemical composition of regular PTR glass consists of a mixture of Na_2O – 4 Al_2O_3 – 70 SiO_2 – 5 NaF – 5 ZnO – 1 KBr, with minor amounts of dopants Ce, Ag, Sb and Sn of about ~ 0.01 % mol. This means that the glass consist in a SiO_2 matrix with an addition of Na_2O, ZnO and Al_2O_3 that act as network modifiers. On the other hand, the role of NaF and KBr is crucial for the photo-thermo-crystallization process that takes place in the thermal development stage. Those compounds are the main agents involved in the nucleation process and further crystal growth. KBr also acts as a batch condenser or 'flux' decreasing the temperatures needed for the glass melting operation making the process more energy efficient. Cerium and silver are fundamental ingredients of PTR glass as they serve as photosensitive agents absorbing the actinic radiation and activating the chain of photochemical reactions. Antimony also plays a role as a thermo-reducing agent, trapping electrons released from Ce^{3+} in the photoionization process and trapping by Sb^{5+} complexes [17]. These electrons trapped by Sb^{5+} complexes are then released in the following thermal development stage to be trapped by the remaining Ag^{+} ions contained in the UV irradiated areas. Antimony is also a

fining agent that prevents bubbles forming during the glass melting process. Finally, tin is added as fining agent of the glass that also participates in oxygen (O_2) removal processes.

Another of the main properties of PTR glass is the glass transition temperature (T_g). This property can be seen as the temperature at which the glass transforms from elastic to plastic media and structural transformations start to occur. The most preferable method for measuring the transition temperature of glasses is using differential scanning calorimetry (DSC) techniques [18]. For PTR glasses of standard composition, the transition temperature is found in the vicinity of 470 °C. Through the DSC technique is also possible to measure the crystallization temperature of glasses (T_x). Spontaneous crystallization of PTR glass occurs at temperatures around 650 °C. Whereas induced crystallization effects that take place after exposure of this glass to UV irradiation start to occur in the range of 550 °C.

The thermo-mechanical properties of the glass like viscosity, mechanical relaxation and elastic moduli have been also explored in [19]. Here it was estimated that the elastic properties of the glass remain practically unaltered within a temperature domain of 293 °K to ~ 523 °K. To find the timescale τ_α of structural (α-) relaxation linked to the transition regime of the glass the authors used the elastic constants along with the Newtonian viscosity of the medium. In elastic media, two modes were found using dynamic-mechanical thermal analysis (DMTA): β and γ. Moreover, it was determined that β- and γ- modes yield longer times and higher temperature values in comparison to a ternary sodium silicate glass, which is a reference glass of comparable viscosity properties [19]. Such results allowed the assumption that fluorine and oxygen exist in the medium and decelerate the motion at non-bridging oxygen locations.

Comparison of obtained data in [19] showed that activation energies and decoupling rations for the β- and γ- modes are relatively of the same order than in trisilicate glasses but PTR relaxes slower. This slower relaxation could be explained given that local structural

arrangements will be delayed with respect to the trisilicate glass due to the higher chemical complexity of the multi-component PTR glass.

1.7 General mechanism for RIC in PTR glass

It is well known that PTR-like glasses exhibit coloration [1] and a permanent and localized refractive index change [5] after exposure to actinic UV radiation and subsequent thermal treatment above the glass transition temperature. Furthermore, it has been demonstrated that heating of these glasses at temperatures above T_g results in the precipitation of sodium-fluoride crystals. A detailed description of the complex mechanism of photo-thermo-induced crystallization for coloration of PTR-like glasses can be found in [20]. Several publications more report on the evolution of the material structure and its optical properties triggered by exposure to UV light and further thermal treatment as well [21, 22]. However, despite the numerous publications on PTR glass photoinduced properties and its development to commercial stage, the origin of the local refractive index change is still under investigation. Given the complexity of such multicomponent silicate glass, it is not clear which particular species and transformations are responsible for the refractive index decrement that is observed. Therefore, to understand better the mechanism of this phenomenon a step-by-step analysis of the process is necessary and will be presented in the next sections of Chapter 1.

1.7.1 RIC by photo-thermo-refractive process

The first observations of RIC by means of a photo-thermo-refractive processing was in Li_2O-Al_2O_3-SiO_2 glass matrix doped with Ag and Ce. It was observed that after exposure of the glass to a mercury lamp [23] followed by thermal treatment generated Ag colloidal particles that changed the color of the glass sample. Here it was found that prolonged thermal treatment

of the glass caused even stronger coloration, and that RIC was produced by lithium metasilicate (Li_2SiO_3) crystalline structures. It was also detected that the surface profile in the glass area exposed to radiation was modified by shrinkage. Such shrinkage was dependent on the conditions of exposure and heat treatment and could manifest itself as surface undulations (peaks and valleys) that ranged from 1 to 10 μm. In this case, both glass volume shrinkage and RIC were attributed to a higher concentration of crystals as compared to the one in original glass, and also that the chemical composition of the residual glass (with crystalline phase) was modified. Researches in 1949 [1] by Dr. Stookey et al. led to the discovery of photosensitive opal glass, where a monochromatic image formation by coloration was demonstrated. This coloration was caused by the absorption and scattering resulted after precipitation of several types of crystalline phases including NaF after UV exposure and thermal treatment. More studies revealed [20] that a second exposure of this material after heat treatment to UV light exhibited a dependence of coloration on dosage of UV exposure and thermal development regime. Therefore, a polychromatic image could be generated in the bulk of the glass. A chain of processes that include the following steps explained such capacity for coloration or 'photosensitivity' of this polychromic glass.

First exposure of a polychromatic glass to UV radiation caused photoionization of Ce^{3+} ion (this process is explained in detail in Chapter 2) into Ce^{4+}. The released electrons are then captured by Ag^{+} ions converting them into neutral atomic state Ag^{0}. Second, when the glass is heated up to temperatures beyond 400 °C after being exposed the formation of sub-nanometer silver aggregates (clusters) that serve as nucleation centers starts. Third, further heating to temperatures above 500°C of the previously nucleated sample resulted in precipitation of sodium fluoride nanocrystals that grow on the Ag centers. Additional exposures and thermal treatments resulted in the precipitation of elongated Ag crystals on the top of NaF crystals. The

absorption spectrum of such enlarged structures depends on their aspect ratio that is determined by the level of the additional exposure [20].

PTR glass belongs to the same family of photosensitive media, and it has been demonstrated that it shows not only color change but also significant refractive index decrements down to 10^{-3} (1000 ppm) after the first exposure and thermal development [24]. Similar to the lithium-aluminum-silicate glass, RIC was interpreted as a higher density of crystalline phase (sodium fluoride grown on silver bromide particles) and by changes in the chemical composition of residual glass.

Thus, let us propose the simplified model for the refractive index change in PTR glass. First, glass is irradiated with near UV light producing photoexcitation of the Ce^{3+} ion from the ground state into its 5d1 band and released electrons are captured by Ag^{+} transforming it to Ag^{0} (Figure 1.6 a). Second, the glass is heated up to temperatures above the glass transition temperature (T_g = 470 °C) causing silver atoms to diffuse and create silver clusters as shown in Figure 1.6 b. Third stage involves further heating at temperatures above 500°C, where the silver clusters serve as nucleation centers for the NaF nanocrystals growth. However, despite the reliability of the photo-thermo-refractive process to induce refractive index changes needed for holographic recording recent studies [25] have revealed that the mechanism of refractive index change goes beyond the simple concept of crystalline phase density.

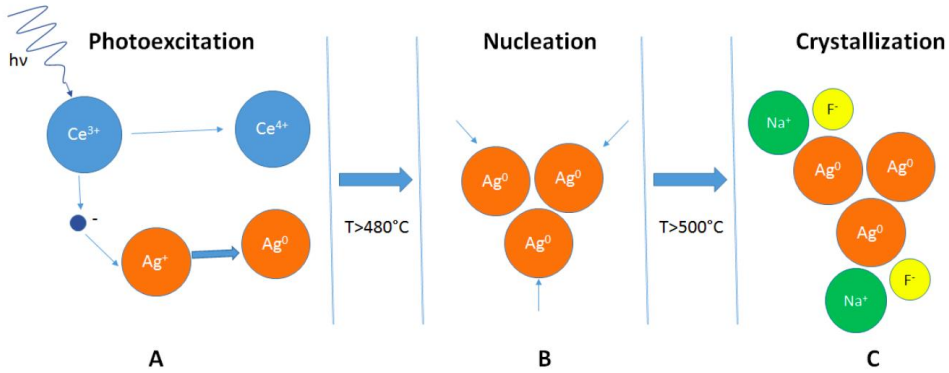

Figure 1-6 Stages of the photo-thermo-refractive process

1.7.1.1 UV exposure and color center generation

RIC in PTR glass depends on the UV exposure dosage as it is shown in Figure 1.7. This dependence obeys the Reciprocity law, meaning that regardless of the light intensity or exposure time the same values of induced refractive index will be obtained for the same dosage.

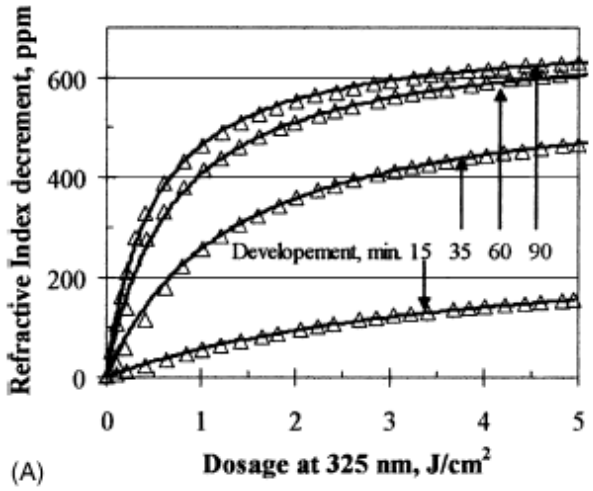

Figure 1-7 Dependence of RIC on dosage for different development times at temperature of 520 °C in PTR glass [26]

After performing accurate measurements of RIC for a number of regimes of exposure (dosage levels) and thermal treatment times, this allowed the possibility of fitting this data to mathematical models [26]. It was revealed that the most accurate modeling of the behavior is achieved by using a hyperbolic function of the type:

$$\Delta n = \frac{\Delta n_s E}{\varepsilon + E} \tag{1-2}$$

Where Δn is RIC, E is UV dosage, Δn_s represents maximum value of RIC when it reaches saturation at an infinite dosage, ε is a dosage required to reach $\Delta n = 0.5 n_s$ (which is half of the saturation dosage). In next Figure 1.8 we can observe the maximum RIC (n_s) and half-max saturation dosage (ε) plotted versus development time at a fixed temperature of 520 °C. We can notice that n_s reaches saturation after 60 minutes of heat treatment and reaching 600 ppm meanwhile ε decreases down to 0.5 J/cm^2 as the development time is increased 90

minutes. This means that the dependence of RIC on the provided dosage can be treated as a linear correlation for low development times, then quasi-linear with an asymptotic trend towards a saturation point for increased development times.

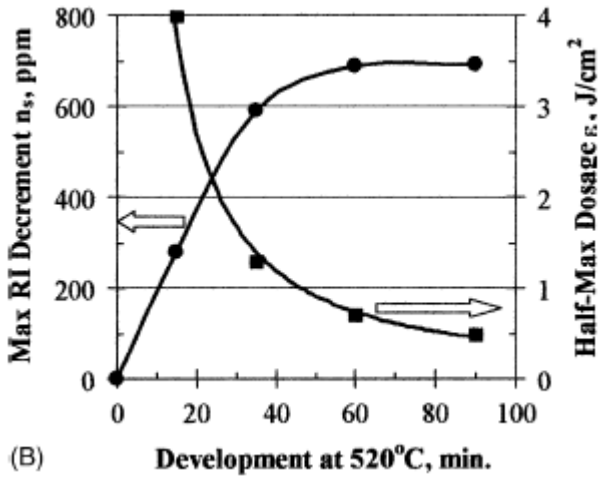

Figure 1-8 Dependence of maximum RIC and Half-Max dosage on development time at temperature of 520 °C [26]

A meticulous investigation [22] of RIC in PTR glass under a liquid cell shearing interferometer showed that UV exposure at room temperature originated not only additional absorption in the UV and visible regions but also caused a small refractive index increment in the glass of 5 ppm. In Figure 1.9 (left), we can observe refractive index profiles of a sample irradiated with a Gaussian beam (TEM_{00} mode) from a 325 nm He-Cd laser for dosage levels of 600 mJ/cm^2 and 115 mJ/cm^2. Such small RIC of 5 ppm could be explained by an increment in the size of centers that, at the atomic level, trap the electrons released by Ce^{3+} in the photoionization process (this is generation of color centers) [27, 28]. One of the suppositions is that a volume increment after UV exposure compress the areas bordering the atomic centers and that this effect translates into a refractive index increment. It was demonstrated [27, 28] in undoped silicate glasses that heating to several hundred degrees Celsius resulted in restoration of refractive index to its original value due to thermal destruction of the color centers or also called “bleaching”. On the other hand, bleaching of color centers can be achieved through high-power optical radiation as well [29].

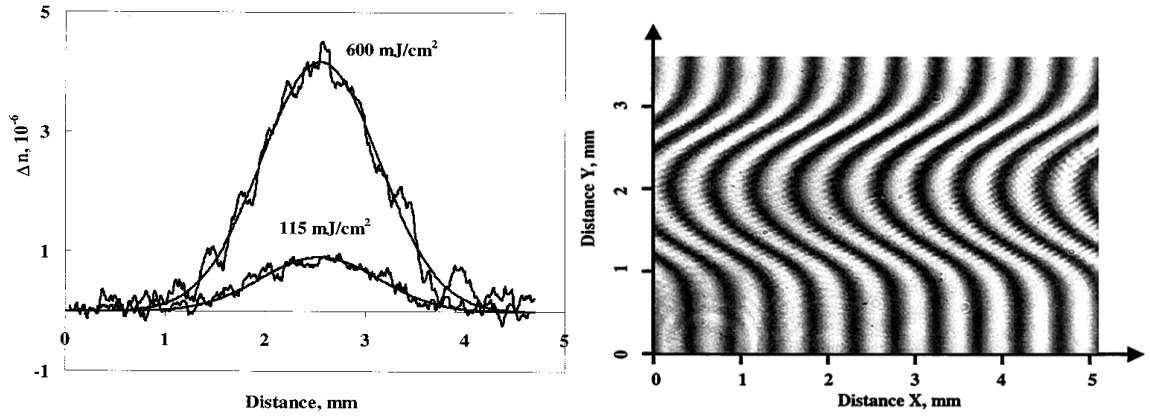

Figure 1-9 Induced refractive index profile of PTR glass exposed to 325 nm for 115 and 600 mJ/cm^2 (left) and corresponding shearing interferograms showing a Gaussian lateral stripe produced by scanning beam of 325 nm laser for 600 mJ/cm^2 followed by thermal development for 2 hours at 520 °C (right) [22]

1.7.1.2 Thermal development, nucleation and crystallization

Another macro-structural transformation observed in PTR glasses after UV exposure and thermal treatment is an increment in the volume of the glass also known as 'glass swelling' [30]. It was observed in this works that samples exposed to 325 nm UV radiation and thermally treated at 520 °C, exhibited an elevation on their surface profiles in the exposed areas with respect to the non-irradiated parts. The samples underwent irradiation of UV Gaussian stripes from 0.25 mm to 3 mm width and subsequent thermal treatment at 520 °C. It was observed that exposed regions in a 1 mm-thick sample exhibited an elevation of 300 nm as shown in Figure 1.10. An interesting feature is that the same elevation was distinguished in the backside of the sample as well [30].

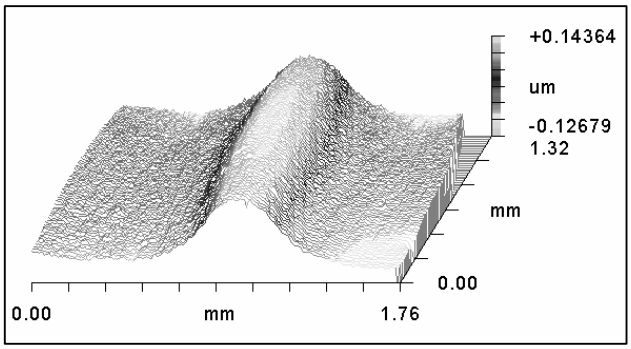

Figure 1-10 Spatial profile in three dimensions of the elevation of PTR glass sample after exposure to UV Gaussian stripe at 325 nm and thermal development [30]

These results brought the conclusion that volume of glass in the exposed regions becomes larger and that there is a relative volume change of 6×10^{-3} as compared to the unexposed zones. Interestingly, this value is near to the maximum value of achievable RIC in PTR glasses (1000 ppm). Due to this results, the hypothesis that RIC could be due to lower density of the glass in the regions exposed to UV irradiation was born. In the same works [30] it was assumed that the precipitation of NaF nanocrystals could provide an explanation to the volume gain in exposed areas. As it was explained before in section 1.6.2 crystals are generated above T_g when the glass transforms from elastic to plastic state. It is explained here that depletion of Na and F ions in the residual glass occurs when crystals are formed and that this will have an effect in the coefficient of thermal expansion since the fluorine concentration decreases. This will mean that when glass is cooling down in the development process the regions where NaF nanocrystals precipitated will shrink slower than the area with no crystals [30].

The relationship between RIC and concentration of sodium-fluoride crystalline phase was investigated by measurements in a liquid cell shearing interferometer and X-ray diffraction (XRD) using the same set of PTR glass samples [31]. These XRD studies showed that crystallized PTR glass exhibited X-ray diffraction peaks at 39, 56 and 70.5°. It is shown in this research that by comparison of intensity of the main XRD peak of NaF at 39° the concentration of NaF nanocrystals can be retrieved for PTR glass samples that underwent different regimes of UV exposure and thermal development. Crystallized samples were compared with a mixture of PTR glass in powder form using its standard batch components and different concentrations of NaF powder [31]. In the measurements was observed that the concentration of NaF crystals in PTR glass samples that underwent standard development conditions necessary for holographic recording (0.9 J/cm^2 at 325 nm and 520 °C for 1 hour) reached 0.1 wt % and no that other type of crystalline structure was detected. Nonetheless, XRD in completely

crystallized sample developed at 600 °C for 15 hours contained small amounts of KBr crystals. In conclusion, it was found in these studies that there is a linear correlation present between the concentration of NaF and RIC (Figure 1.11 left).

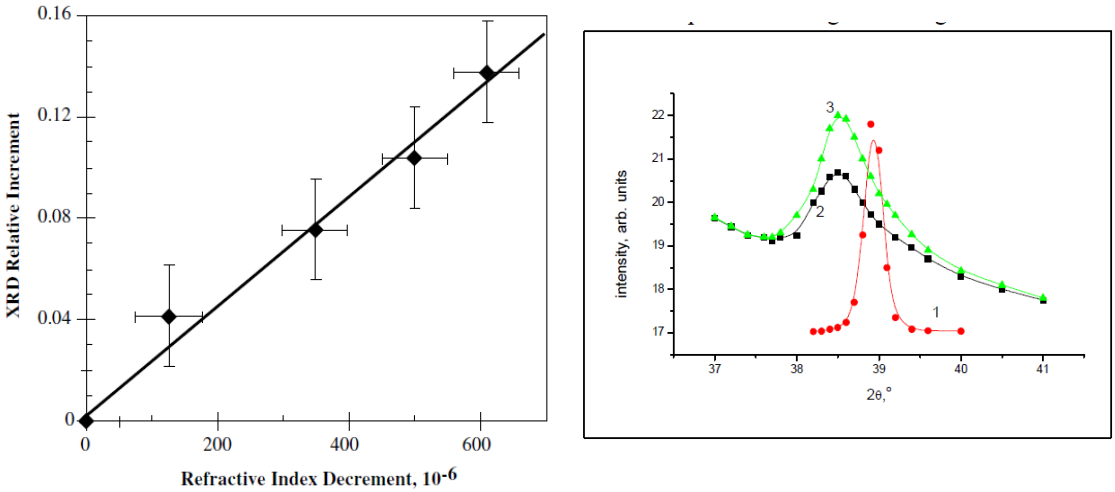

Figure 1-11 Correlation between XRD relative increment and refractive index decrement (-Δn) in PTR glass exposed to UV radiation at 325 nm and developed at 520 °C for 1 hour (left) [31]. X-ray diffraction of NaF powder (1), PTR glass with a recorded hologram (2), and PTR glass exposed to X-rays and developed at 510 °C for 2 hours (right) [32]

Further researches studying the mechanism of RIC in PTR glass was demonstrated by study of small-angle X-ray scattering (SAXS) [32]. The appearance of small concentration of amorphous centers of about 2 nm size was detected. This was concluded by the measurement of a scattering peak of about 40 mrad. It was found that if the glass is exposed to ionizing radiation the number of the amorphous centers increased whereas their size decreases. Moreover, thermal treatment at 520 °C showed crystalline phase precipitation of centers with sizes about 15 nm and an additional amorphous phase of about 5 nm size. Moreover, thermal development at 420 °C modified the amorphous phase of 5 nm but did not alter the phase of crystalline structure [32].

Studies on the effects of thermal development on the crystallization kinetics of PTR glass were performed in [33]. The findings showed that PTR glass exposed to UV radiation and developed for 20 min. at 500 °C shows a different RIC when is slowly cooled down to room temperature opposed to another one rapidly quenched. In Figure 1.12, we can see dependence of a relative RIC on quenching temperature. Here, one can observe that RIC grows as the temperature before quenching reaches 420 °C.

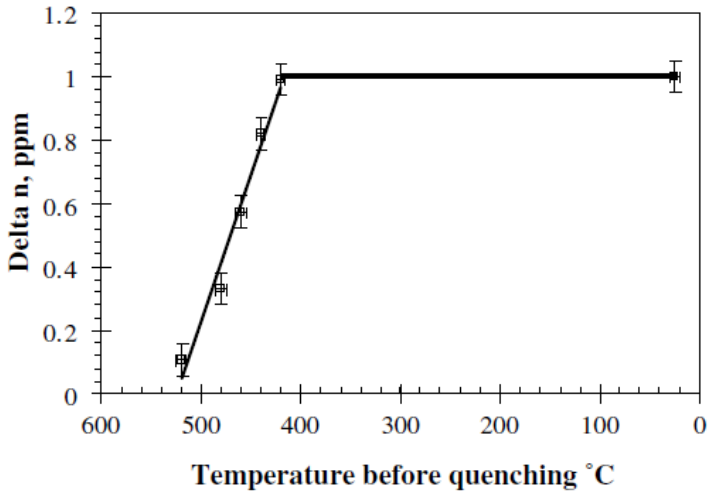

Figure 1-12 Dependence of relative RIC of PTR glass on temperature before quenching [33]

These results pointed out for the possibility that RIC does not take place in the course of development at 500 °C but during the slow cooling process that happens between 500 °C and 420 °C when a samples is reaching the room temperature. This will mean that the nucleation centers needed for holographic recording are not a product of sample dwelling at a fixed temperature but throughout the subsequent slow cooling process.

More experiments studying other mechanisms of RIC as a consequence of the precipitation of NaF nanocrystals in PTR glass was presented in [25]. In this case the three main considerations that contributed to RIC were: (1) distribution of Na and F in both crystalline and amorphous phases, (2) difference in the specific volume of glass in exposed and unexposed areas and (3) stresses generated in different regions after thermal development. These studies were performed using a refractive index for NaF crystals of 1.32 and 1.49 for pristine PTR glass. The main idea was to verify if Na and F refractive indices were different in glass and crystalline phases, refractive index of ceramic glass would be different from the one in pristine form (single phase with no crystals). As an attempt confirm this, samples of 3CaO-22Na_2O-75SiO_2 glasses with partial replacement of Na_2O to 2(NaF) were prepared to measure their refractive indices.

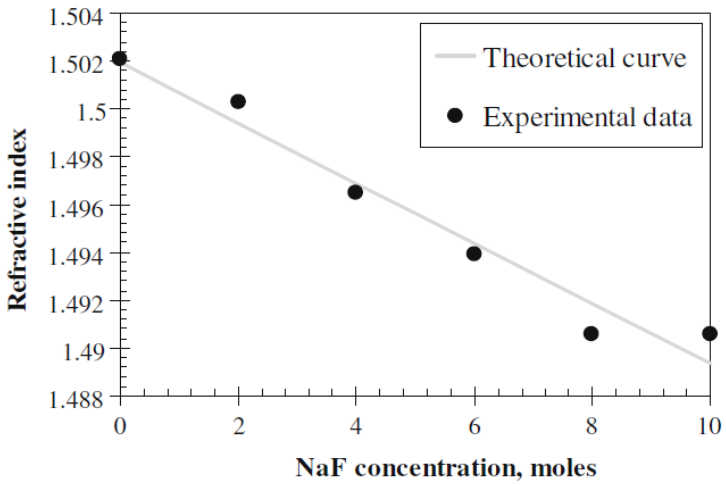

Figure 1-13 Refractive index of soda-lime silicate glass on concentration of NaF [25]

It can be observed from Figure 1.13 that if the concentration of fluorine in the samples increased the overall refractive index of glass was decreasing. Then, the authors modeled the correlation with Demkina method [34] using partial constants of different oxides that were used to prepare these optical glasses obtaining the following expression:

$$n = \frac{\frac{a_{CaO}}{s_{CaO}} n_{CaO} + \frac{a_{SiO_2}}{s_{SiO_2}} n_{SiO_2} + \frac{a_{Na_2O}}{s_{Na_2O}} n_{Na_2O} + \frac{a_{NaF}}{s_{NaF}} n_{NaF}}{\frac{a_{CaO}}{s_{CaO}} + \frac{a_{SiO_2}}{s_{SiO_2}} + \frac{a_{Na_2O}}{s_{Na_2O}} + \frac{a_{NaF}}{s_{NaF}}} \quad (1\text{-}3)$$

Here a_i is a weight concentration, s_i represents molar weight, and n_i is partial refractive index of the species. Since n_{NaF} was the only unknown in the equation the authors fitted the experimentally obtained value for total refractive index showed in Figure 1.13 and solved. The value for n_{NaF} was then found to be 1.34 ± 0.03 which is very close to refractive index of NaF crystals. This means that refractive indices in crystalline and non-crystalline phases get counterbalanced to each other.

In order to visually investigate the change of refractive index for discrete temperatures, PTR glass was exposed to UV and thermally developed to record a Gaussian stripe pattern across a sample in [25]. The sample was placed inside a thermal cell in one of the arms of a Michelson interferometer while it was monitored when heat was applied as shown in Figure 1.14. It was observed that at room temperature the interference pattern seems like a normal Gaussian fringe shift due to UV laser beam profile used for irradiation. There was no detectable effect when the sample was heated at temperatures lower than T_g. Surprisingly, when the sample was heated beyond 450 °C the pattern produced by the Gaussian stripe completely disappeared [25]. This result signifies that at this point the refractive index change difference between exposed and unexposed regions was eliminated and the remaining contours are just the product of small optical distortions. The interpretation that the authors gave in this case is

that huge stretching stresses between crystals and glass create a RIC that disappears above T_g and is restored when the sample returns to lower temperatures.

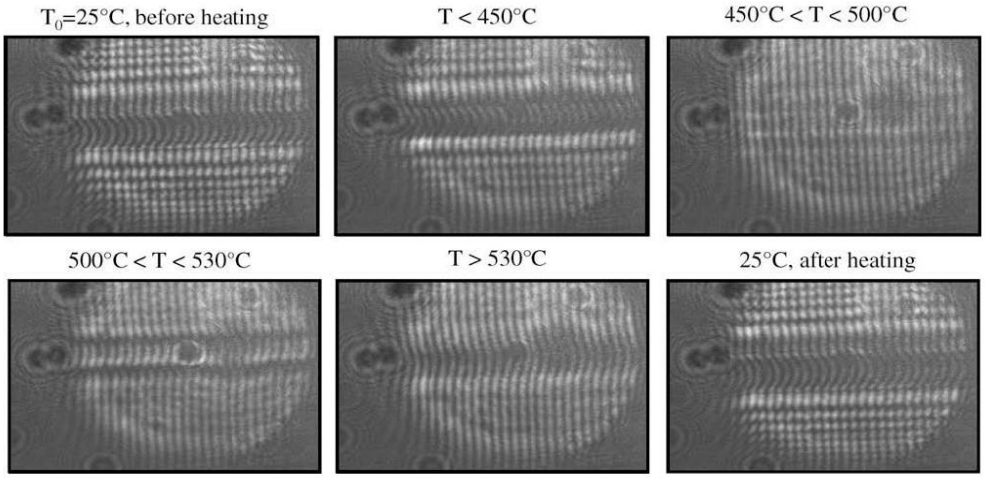

Figure 1-14 Interferograms of a PTR glass sample exposed to a 1-mm-thick Gaussian stripe of radiation at 325 nm and developed for 1 hour at 515 °C [25]

Since the works shown in [25] needed an explanation to the elimination of RIC at temperatures beyond T_g and its restoration when returning to room temperatures a new research review proposed a triple phase system (for exposed and developed glass) like the one depicted in Figure 1.15 (left) [25, 35]. This model takes in account that a vitreous region depleted of NaF surrounds NaF crystals and both of them live in turn in an unperturbed PTR glass phase. The central idea is that between the T_g of the unperturbed glass (460 °C) and the induced crystallization temperature of 515 °C, the expansion (or volume change) of the different phases in the triple-system occurs at a different rate as depicted in Figure 1.15 (right) [35]. In this way, it was possible to explain why the RIC is not altered below T_g and elimination of refractive index difference between irradiated and non-irradiated regions above T_g. Despite all these efforts, the effect of stresses for each interface of the three-phase model described above is not completely understood yet and further investigations are needed.

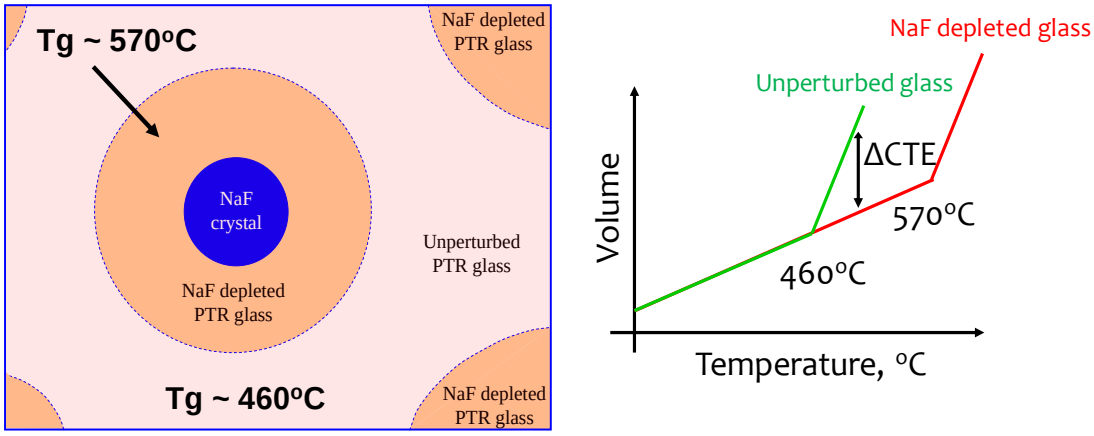

Figure 1-15 Schematic of triple phase structure (left) and dependence of specific volumes of vitreous phases on temperature (right) for PTR glass after UV exposure and thermal development [25, 35]

New TEM techniques allowed the study of pristine and uniformly irradiated PTR glass [36]. The research showed that a sample irradiated with dosage of 1 J/cm^2 at 325 nm and thermally treated at 515 °C during 1 hour precipitated crystals with cubic form of about 15 nm in size with joint pyramids of 80 nm long and 10 nm width. A very important observation was that a longer development times only caused the growth of the cubic crystals in size but the number of crystals remained the same. In Figure 1.16 we can observe TEM micrographs of the samples used in these experiments showing how the size of the crystalline cubes increases as the temperature of development goes higher [37].

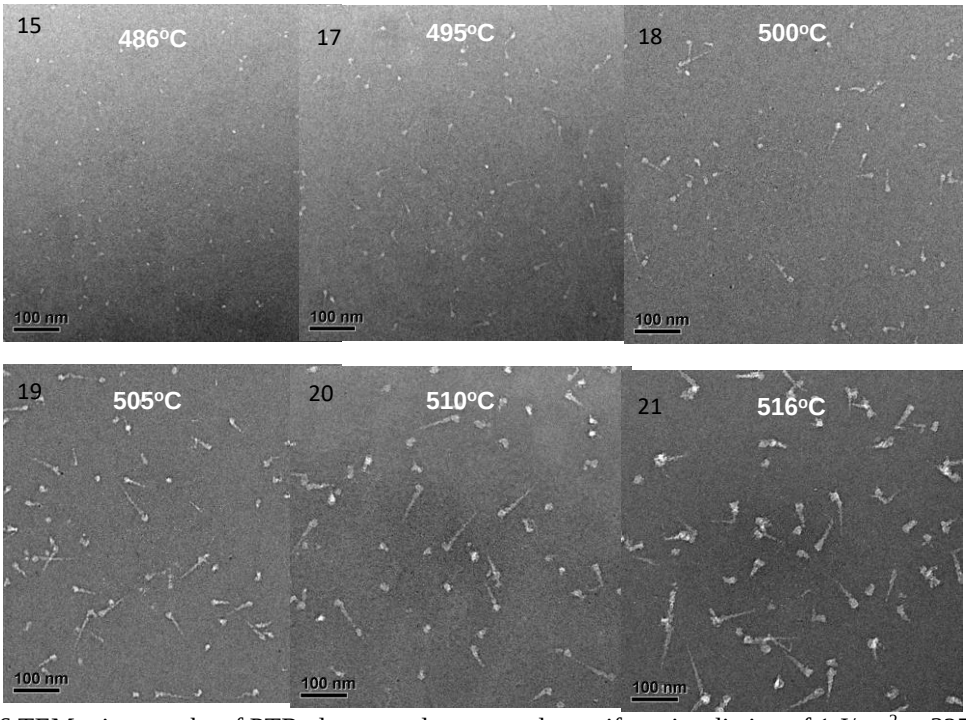

Figure 1-16 TEM micrographs of PTR glass samples exposed to uniform irradiation of 1 J/cm^2 at 325 nm and nucleated for 485 °C for 60 min. and developed at different temperatures for 60 min [37]

From the information provided in the TEM micrographs the authors of [37] obtained a graphic description of the correlation of crystallization parameters with temperature and are presented in Figure 1.17. As explained before the results show that the number of crystals is independent from the thermal treatment temperature. Hence, concentration is controlled by UV exposure and generation of nucleation centers. Moreover, the size of the cubic formations is dependent on the development temperature. With the use of these experimental data [37], one can depict the dependence of RIC of the same sample on thermal development and such function corresponds to a cubic parabola. Therefore, after UV exposure the RIC in these samples is equivalent to cube of thermal treatment temperature and proportional to the concentration of NaF nanocrystals. Nevertheless, as we explained before the role of NaF nanocrystals is very complex and more studies are necessary to break down the complete mechanism for RIC in PTR glass.

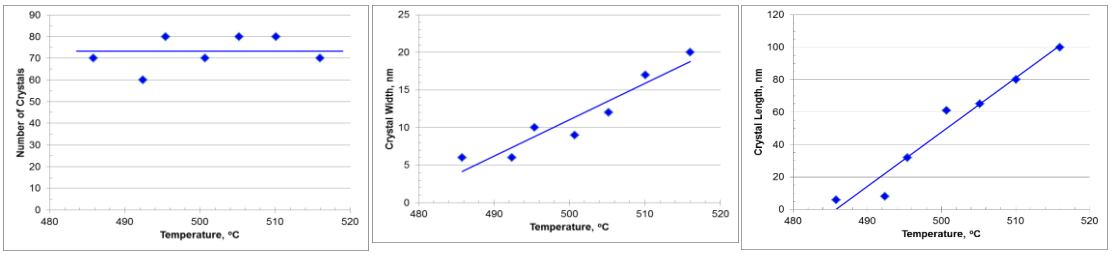

Figure 1-17 Dependence of crystal parameters on temperature of thermal treatment for PTR glass exposed to 1 J/cm^2 at 325 nm nucleated at 485 °C for 1 hour and developed for 1 hour [37]

1.8 Spectroscopy and thermal studies of samples with different Bromine concentrations

One of the agents that is mainly involved in the structural transformations of PTR glass is Bromine. It has been demonstrated [38] that the concentration of Bromine is directly correlated with the RIC that appears after UV exposure and thermal development. Moreover, in the same works was shown that the concentration of Bromine has a strong influence in the NIR absorption band of PTR glass (~2.7 μm) since this is one of the bands mainly related to water (O-H groups) absorption. Also, it was shown that the UV-VIS part of the spectra exhibits a shift in the position of its Ce^{3+} and Ce^{4+} band due to a change in the redox conditions within the material [38].

This study was continued in this dissertation work. Several samples with different concentrations of Bromine were synthesized and their optical absorption spectra were measured using PerkinElmer UV/VIS Spectrometer (model: Lambda 950) with resolution of 1 nm. The Bromine glasses under study contained 0, 25, 50, 75, 100 and 150 % of the normal Bromine concentration used in PTR glasses. Therefore, plots displayed in figures of this section are labeled accordingly. The measured absorption spectra for these glasses in the NIR region is shown in next Figure 1.18.

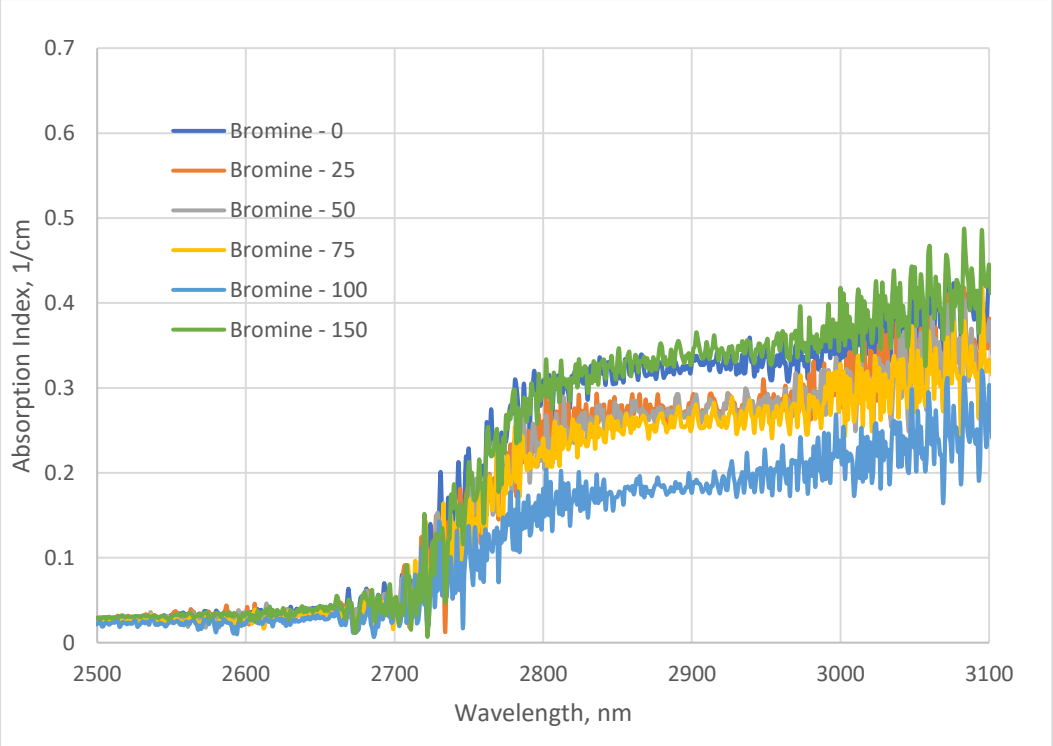

Figure 1-18 NIR absorption spectra of Bromine glasses

These measurements match with the observations from Glebov et al. [38] where the concentration of Bromine was inversely proportional to the level of water absorption. This statement is valid in all our measurements except for the sample containing 150% of Bromine concentration. Some of the hypothesis for the inconsistency at 150 % may be related to competitive processes between Bromine and Fluorine occurring in the glass at concentrations higher than 100% of Br. Since both species (Br and F) are in chemical competition for hydrogen-compound formation (HBr / HF) that can be very volatile [39] the water concentration in the absorption spectrum of PTR glass could be changed. Other component that can be closely related to bromine is Ag. It is described in [40] the close relation between Ag and Br and how it can have an influence on the optical absorption spectra of photochromic glasses.

In addition, measurements on the UV/VIS part of the spectra confirmed that the spectrum of PTR glass exhibits a shift of its Ce^{3+} band with maximum at 305 nm for different concentrations of Br as shown in Figure 1.19. As mentioned before, one of the reasons for this change is the chemical competitiveness between bromine and fluorine in different types of redox processes occurring during the glass melt. If bromine somehow affects the redox dynamics of fluorine, a change in the position of maxima in the Ce^{3+} band will be expected.

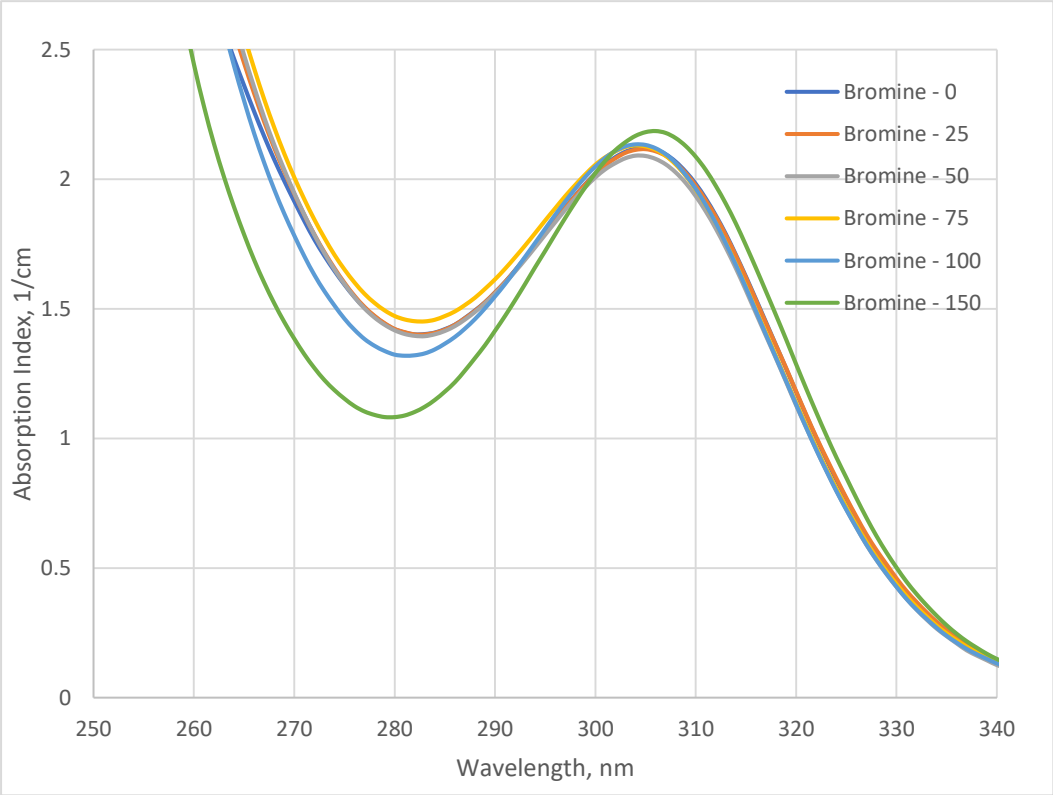

Figure 1-19 UV absorption spectra of Bromine glasses

Now, in order to study the effect of Bromine on the thermo-mechanical properties of PTR glass twelve samples (two for each concentration) were measured using the DSC technique explained in previous sections and their value of T_g was calculated. The calculated values of T_g were subsequently plotted versus the Bromine concentration obtaining the following results.

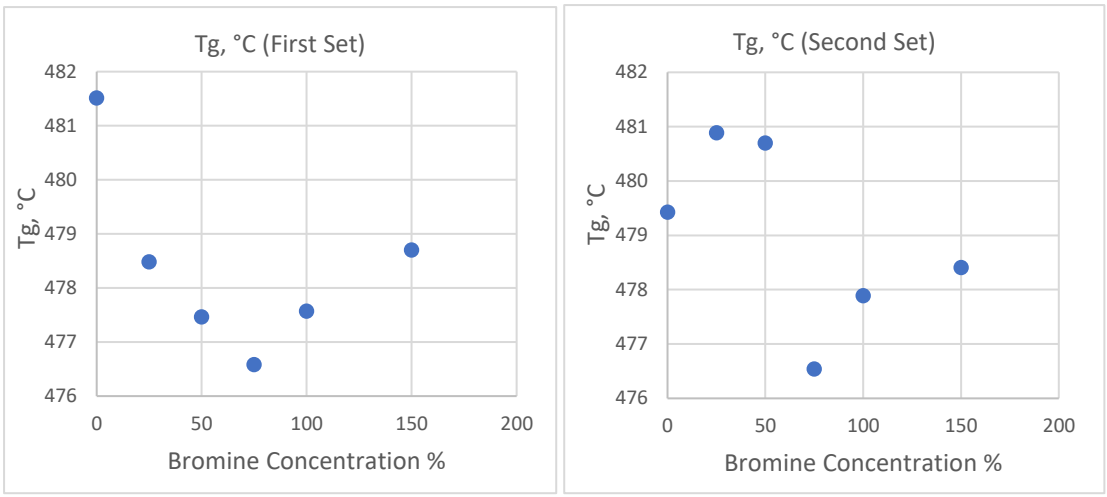

Figure 1-20 Dependence of T_g on the Bromine concentration of PTR glass samples used in the experiment. First (left) and second (right) set of six measured samples

As we can observe from Figure 1.20, the dependence of T_g versus Bromine concentration in both sets of samples resembles to that of a eutectic system where a binary chemical mixture is melted at temperatures lower than the melting point of the single isolated components [41]. This effect has never been reported on PTR glass previous studies to the best of our knowledge and further studies have to be undertaken to provide more detailed conclusions. In summary, it was proved that Bromine has a direct effect on the NIR absorption band of PTR glass. Moreover, that the position of the Ce^{3+} maximum is dependent on the Br concentration. An effect that resembles that of a eutectic system was found at a point of 75% of Bromine concentration in two different sets of PTR glass samples. These measurements open a possibility of chemical tuning of the T_g by changing the Bromine concentration in PTR glass composition.

CHAPTER 2: PHOTOIONIZATION PROCESSES IN PTR GLASS

2.1 Introduction

The phenomenon of interaction between light and matter is normally studied as excitation of electrons from their ground state to higher levels in their interatomic configurations. When photoexcitation of electrons from discrete energy levels of PTR glass dopants occurs, electrons are generated in the conduction band of the material with energies close to their electron mobility threshold. Generation of a mobile electron also creates a hole pair that along with their mutual confinement and recombination can be considered as the foundation of photoionization processes in PTR glass [42]. To investigate such phenomena, we study the optical absorption and photoluminescence spectra. These effects will be studied on PTR glass (mol %: $71SiO_2$-$13Na_2O$-$3Al_2O_3$-5ZnO-6NaF-2KBr) activated with individual dopants (or a specific combination) by measuring their optical properties using specialized UV/VIS and Fluorescence spectrometers. However, several challenges are faced during these measurements. One of the main problems is the natural overlapping of the absorption and emission spectra of the PTR glass dopants. To overcome this issue several experimental glasses containing only specific dopants were synthesized. It will be presented a study of PTR glass matrix (Glass ID: D0) and glass matrix doped with Sn (Glass ID: D3) that we will call from now on as 'D-glasses'. Specifically, we will investigate the optical properties of D0 (glass matrix + Fe^{3+} impurities) and D3 (glass matrix + impurities doped with Tin).

Finally, to expand our knowledge on the study of phase transformations in PTR glass we performed optical absorption and photoluminescence measurements on pristine, UV exposed and nucleated samples below temperatures of crystalline phase precipitation. Our main

motivation and goal is to catch the initial stage of structural changes to be able to reveal the complete mechanism of refractive index change.

2.1.1 Glasses samples preparation

To conduct these experiments two sets of samples with different thicknesses were prepared using specialized glass processing equipment. The glass ID and corresponding thicknesses for both D0 and D3 sets are presented in Table 2.1. The main reason for different thicknesses needed is to enhance either the absorption of matrix or Fe^{3+} when performing absorption and photoluminescence measurements. This dependence of absorption on thickness and wavelength will be explained to the reader in the next sections of the chapter. In summary, in order to differentiate luminescence signals produced by glass matrix from the ones from Fe^{3+} impurities, the measurements of emission spectra have to be performed at short excitation wavelengths $\lambda<215$ nm for glass matrix in thin samples. Whereas the emission spectra of Fe^{3+} ions has to be collected under excitation wavelengths of $\lambda>250$ nm in thick samples.

Table 2-1 Sample IDs and corresponding thickness for D-glasses used in the project

Specification	Sample ID	Thickness, mm
Thin samples	D0	1.056
	D3	0.890
Thick samples	D0	4.954
	D3	1.480

2.2 UV absorption spectra of PTR glass matrix (D0) and matrix doped with Sn (D3)

To define the spectral regions suitable for the optical excitation of PTR glass matrix and Fe^{3+} impurity a deep analysis of the optical absorption of PTR glasses has to be undertaken.

A previous investigation on soda-lime silicate glasses revealed that the primary constituents forming their UV absorption spectral region can be assigned to the intrinsic absorption edge of glass matrix (exponential tail) (1) and absorption band of Fe^{3+} impurity centered at ~ 223 nm (2) [43]. For our experiments, the UV absorption spectra of two types of glasses is compared D0 and D3. The measurements were carried out using a UV/VIS PerkinElmer spectrometer (model: Lambda 950) that allows for a full spectral measurement range of 200 – 3200 nm. As previously explained D0 glass was prepared using PTR matrix only, whereas D3 glass includes matrix doped with a concentration of 0.008 mol % of SnO_2. In this case, Sn was incorporated as a reducing agent with no significant absorption in the wavelength region used in this study. We make this addition under the assumption that Tin would decrease the amount of Fe^{3+} ions by turning them into Fe^{2+}. In accordance to studies of the absorption of iron and water in soda-lime silicate glasses, characteristic absorption of Fe^{2+} ion in this spectral area is an order of magnitude lower than that of Fe^{3+}. In the next figure, we show the absorption spectra of D0 and D3 glasses in the near UV range.

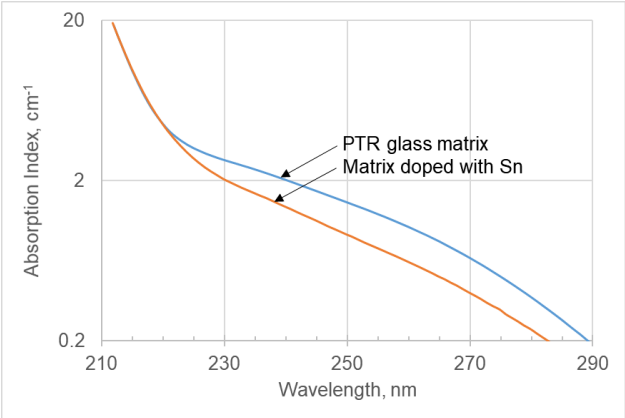

Figure 2-1 UV absorption spectra of D0 (matrix) and D3 (matrix + tin) glasses

We can see that both glasses exhibit absorption spectra similar to the one shown in [43] for soda-lime silicate glasses. Here, a short wavelength edge with exponential behavior and a

broad band centered at ~ 232 nm was observed. If one analyze more deeply it can be found that the spectrum of D3 in the exponential part exhibits a displacement of 0.2 nm towards longer wavelengths with respect to that for D0 glass. Nonetheless, as we are limited by the 1-nm resolution of the UV/VIS spectrometer equipment we suppose that such variation is within the experimental error and can be normally expected. Taking in account this assumption, we can consider that D3 does not change with respect to D0 in terms of shape and position of the intrinsic absorption edge.

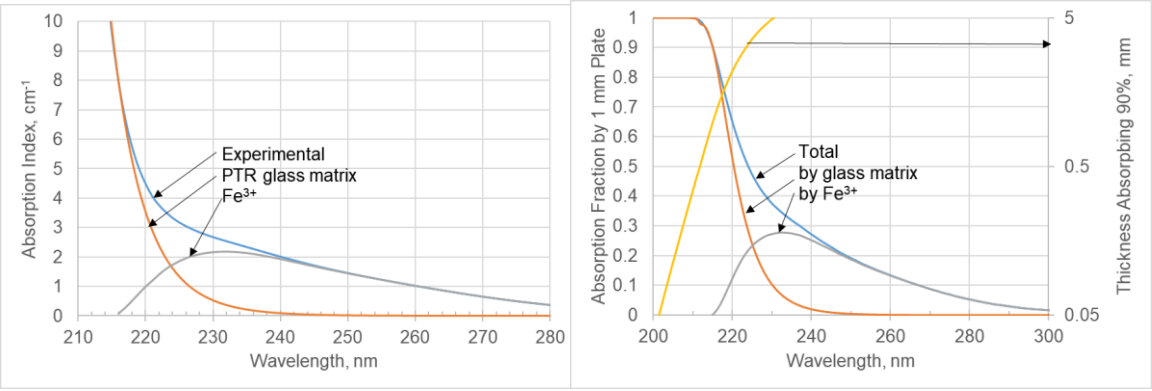

Figure 2-2 Absorption spectrum of PTR glass matrix decomposed in an exponential tail of intrinsic absorption and a wide asymmetric band of impurity absorption (Fe^{3+}) (left). Incident power fractions absorbed by matrix and Fe^{3+} in a 1-mm thick samples along with thickness of layer that absorbs 90% of power (right)

The expression that models the exponential edge of PTR glass matrix shown in Figure 2.2 (orange curve) is the following.

$$A_i = exp - \frac{N_0 - N}{\Delta} \tag{2-1}$$

In this equation A_i (cm^{-1}) represents an absorption index, which can obtained by subtraction of the Fresnel reflection optical density from the optical density losses of the sample and dividing all by the thickness of the sample. The variable N (cm^{-1}) means wavenumber, N_0 represents a wavenumber where $A_i = 1$ (cm^{-1}), and Δ is the slope of the exponential tail. Values found for each of these variables for D0 glass after mathematical treatment resulted to be $N_0 = 44151$ (cm^{-1}) ($\lambda_0 = 226.5$ nm) and $\Delta = 1039$ (cm^{-1}). We can observe in Figure 2.2 that a broad

band (gray curve) related to Fe^{3+} impurities starts to rise around 220 nm. The absorption of this ion is a wide asymmetric band and reaches a peak value of 2.2 cm^{-1} at 232 nm which is double of the absorption found in high purity soda lime silicate glass [43]. Moreover, it was found that absorption of Fe^{3+} impurity is displaced by 9 nm towards longer wavelengths in comparison to the soda-lime silicate counterpart. There is no certainty if this difference is caused by different structure of host glasses or by other unknown contaminations.

In Figure 2.2 (right) it is also depicted the wavelength dependence of absorbed power for different values of sample thickness. We can observe that for wavelengths shorter than 240 nm, 90 % of the power is absorbed in less than 5 mm of the sample's volume. Moreover, one can notice that the fraction of absorbed power for a 1-mm plate increases dramatically below 220 nm due to rise on intrinsic absorption of glass matrix. Thus, the absorbed power for a 1-mm thick PTR glass matrix plate with Fe^{3+} impurities can be described with the following equation.

$$P_a = 1 - 10^{-At} \tag{2-2}$$

In this equation, P_a means fraction of absorbed incident power and t is sample thickness. On the other hand, the absorbed fraction of incident power by a specific constituent can be written.

$$P_{a,c} = (1 - 10^{-At})\frac{A_c}{A} \tag{2-3}$$

The c coefficient is one of the constituents (of D0 or D3) that can be either Fe^{3+} or glass matrix. The same treatment performed for glass matrix was applied to Sn-doped PTR glass samples and the results are displayed in next Figure 2.3.

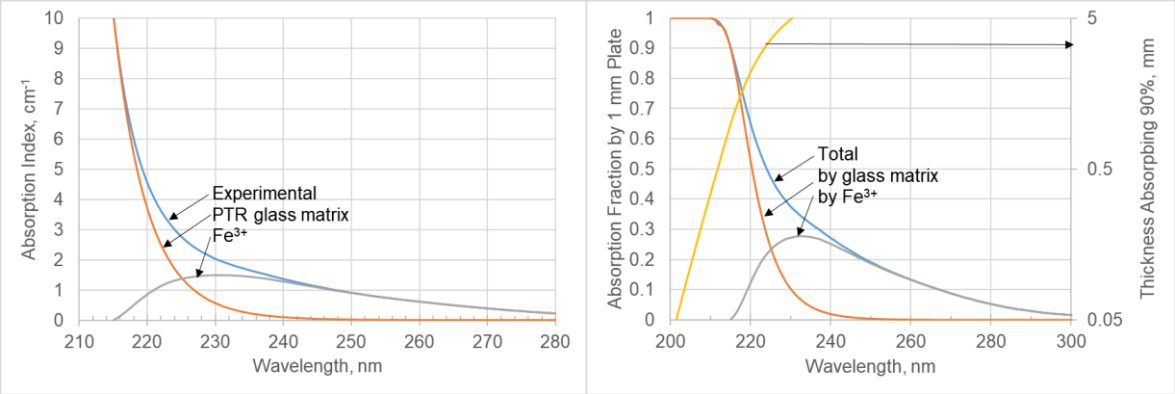

Figure 2-3 Absorption spectrum of PTR glass matrix + tin decomposed in an exponential tail of intrinsic absorption and a wide asymmetric band of impurity absorption (Fe^{3+}) (left). Incident power fractions absorbed by matrix and Fe^{3+} in a 1-mm thick samples along with thickness of layer that absorbs 90% of power (right)

For D3 glass one can notice that for wavelengths λ<215 nm the majority of the power is absorbed by glass matrix and a minimum amount of light is absorbed by Fe^{3+} impurity as we decrease the sample thickness. Thus, we can conclude that the predominant region where Fe^{3+} impurity absorption occurs is λ>250 nm and that a larger amount of light is absorbed by this component as we increase the thickness of the sample. More studies of the absorption and luminescence of PTR glass co-doped with different ions can be found in [44]. In such work, not only absorption, but the DSC and XRD characterization techniques described thoroughly during Chapter 1 were applied.

2.3 Photoluminescence spectra of PTR glass matrix (D0) and matrix doped with Sn (D3)

After analyzing the absorption spectra of D0 and D3 glass samples, we started photoluminescence measurements using PerkinElmer Fluorescence Spectrometer (model LS 45). The spectral resolution of the equipment is 10 nm and allows for an excitation range from 200 to 800 nm. In previous section, we determined that the region most suitable for the excitation of PTR glass matrix and Fe^{3+} impurity was λ<215 nm and λ>250 respectively.

Moreover, we described that in order to distinguish photoluminescence of glass matrix the measurements of emission spectra should be performed using thin D0 and D3 samples. Whereas thick samples should be used when collecting the emission spectra of Fe^{3+} impurity.

Thus, we started the analysis of thin D0 and D3 glass samples by exciting them at wavelengths below 215 nm looking for measurements of photoluminescence of glass matrix. The excitation wavelengths started at 200 nm with increments of 2 nm until a maximum of 215 nm was reached and their emission spectra was collected from 220 nm to 800 nm. In the next Figure 2.4, we observe the luminescence spectra for D0 glass under the excitation range aforementioned. It should be noted that dashed boxes in emission spectra of D0 are signals coming from second order of monochromator inside the equipment and therefore should not be considered as results of this study. The same emphasis was made for the emission spectra presented for D3 glass later on.

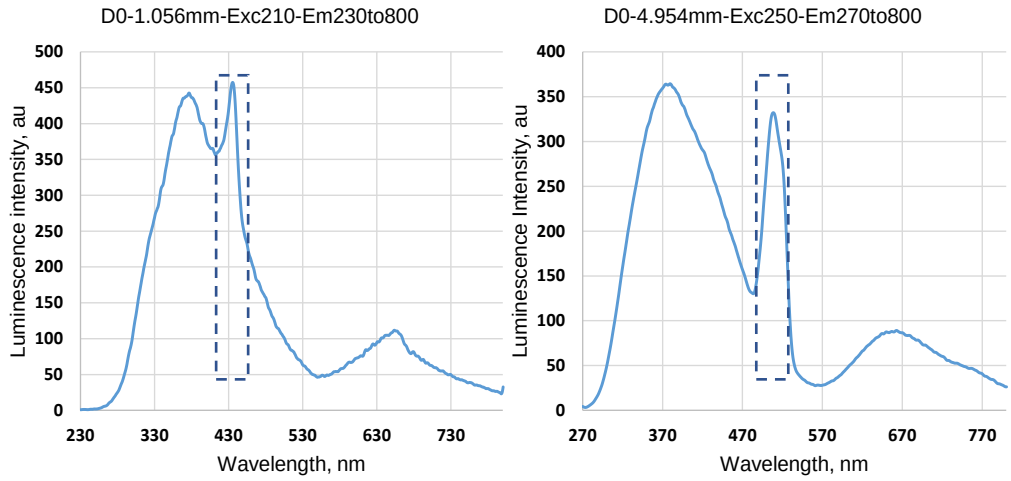

Figure 2-4 Luminescence spectra of thin (left) and thick (right) D0 samples looking for luminescence signals of matrix and Fe^{3+} impurity. Excitation wavelengths are λ=210 nm (left) and λ=250 nm (right)

One can see that under excitation in the range from 200 to 250 nm, the emission spectra of D0 is composed by at least three Gaussian-like envelopes whose wings overlap in a significant range of wavelengths. This overlap in emission spectra complicates the

interpretation of data and does not allow to provide clear conclusions about the emission properties of the glass. The main reason for this signal overlap and possible experimental conditions to correct the results will be discussed in next sections 2.5 and 2.6. Afterwards, we proceeded to repeat the measurements in D3 glass obtaining the following results.

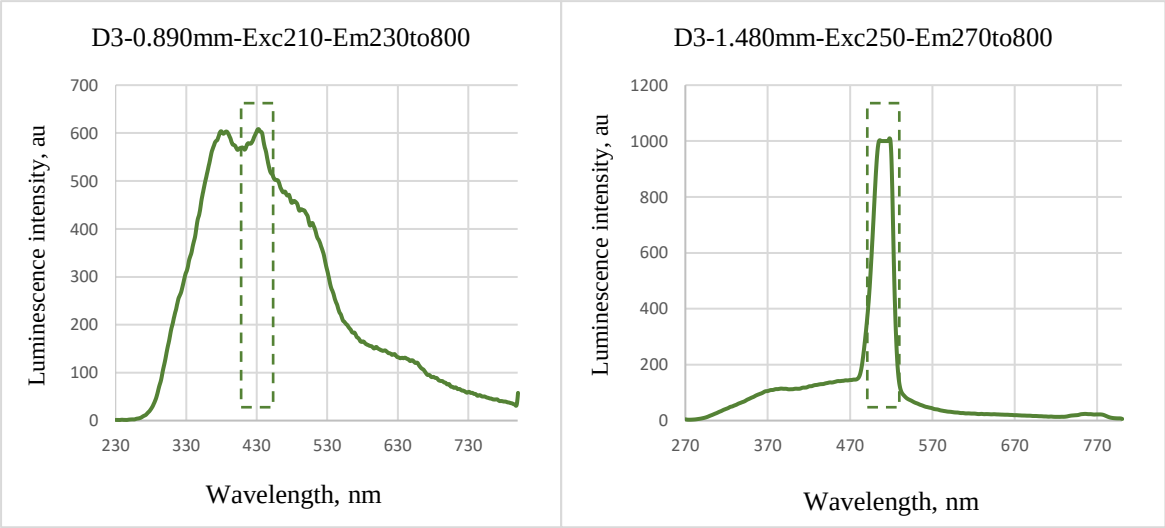

Figure 2-5 Luminescence spectra of thin (left) and thick (right) D3 samples looking for luminescence signals of matrix and Fe^{3+} impurity. Excitation wavelengths are λ=210 nm (left) and λ=250 nm (right)

As we can observe, the emission spectra of D3 glass exhibits a similar behavior than D0 in terms of signal overlapping. The emission spectra for D3 seems to be composed by at least four Gaussian-like envelopes and their overlap is even stronger than its D0-glass counterpart. Therefore, a new experimental approach is necessary to improve the photoluminescence measurements of both D0 and D3 glasses. The improvement of this setup is currently undergoing and will be one of the main goals of the future works of this project.

2.4 Photoionization of Ce^{3+} in PTR glass

One of the key phenomena that triggers the photo-induced transformations of PTR glass is the ionization of the Ce^{3+} ion. This takes place when a UV photon is absorbed by one of its

electrons initially in the ground state that excites into a higher energy level by the transition $^2F_{5/2} \rightarrow 5d$. Detailed spectroscopy analysis of the Ce^{3+} ion embedded in crystalline hosts with known cells allowed to study its electronic transitions with more detail [45]. According to [46] the ground state of trivalent cerium is composed by the doublet $^2F_{5/2}$ and $^2F_{7/2}$ in the 4f configuration. Then, the Coulomb interaction originates the initial ^2D excited state in the 5d electronic configuration to split into two energy levels $^2D_{3/2}$ and $^2D_{5/2}$. Moreover, $^2D_{3/2}$ and $^2D_{5/2}$ levels can be in turn subdivided into five resultant levels if the degeneracy introduced by the spin-orbit interaction along with the crystal field interaction builds up considerably [46]. Therefore, all these interactions can give rise to up to five optical transitions in Ce^{3+}. Five optical transitions were observed for a number of Ce^{3+}-containing crystals and certain phosphate and borate glasses [46]. This indicates that all the aforementioned interactions that cause energy splitting, comprising the one caused by the influence of the crystal field can take place also in the vitreous state. The $^2F_{5/2} \rightarrow 5d$ transition that is responsible for photo-excitation of PTR glass reaches a peak at optical wavelength of 305 nm according to spectral measurements shown in Chapter 1. We have to consider that Ce^{3+} ion accounts for the lowest transition energy (4f-5d) among all rare earth ions (about 4 eV) and therefore for the longest wavelength of excitation [47].

Photoionization of Ce^{3+} involves being transformed to $(Ce^{3+})^{+}$ ion by releasing an electron that either could become an intrinsic color center or reduce other chemical species. Moreover, $(Ce^{3+})^{+}$ ions can transform back to Ce^{3+} by trapping a released electron. It should be noted that in spite of multiple publications, a full description of excitation, luminescence and ionization of cerium in PTR glass was not achieved. Therefore, progress in this direction will be one of the main goals in the next sections of this dissertation.

2.5 Photoluminescence of pristine PTR glass at excitation wavelengths in the UV and visible range

It was found in previous studies that UV excitation of pristine PTR glass causes luminescence of Ce, Ag, and Sb with wide emission spectra having maxima in UV region and long wavelength tails extended to the visible region [48]. No luminescence has been detected under excitation with visible radiation. However, the use of higher power semiconductor laser diode emitting at 405 nm revealed blue luminescence in pristine PTR glass samples (Figure 2.6). Therefore, the analysis of the features of this luminescence under long wavelength excitation are the main objectives of this study. Excitation and emission spectra of luminescence were analyzed using different excitation wavelengths in the visible region.

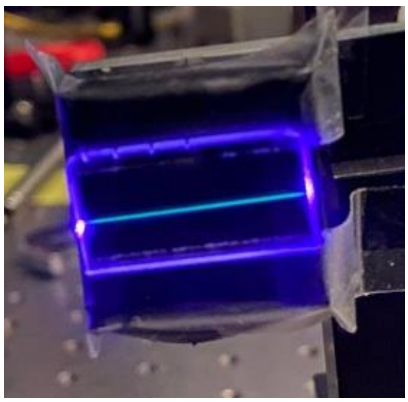

Figure 2-6 Photo of pristine PTR glass sample excited by a laser operating at 405 nm from left to right

For this study, pristine samples of PTR glass with dimensions of 25×25×2 mm^3 and composition (mol.%) $70SiO_2$-$15Na_2O$-$5ZnO$-$4Al_2O_3$-$5NaF$-$1KBr$-$0.01CeO_2$-$0.01Ag_2O$ were prepared for experimental study of luminescence. The procedure for PTR glass fabrication includes a high temperature melting in a platinum crucible with stirring to provide homogeneous samples. Subsequently, the glass is annealed close to its transition temperature in a low temperature furnace and cooled down at 0.1°C/min to increase homogeneity and reduce thermal stresses caused in the fast cooling occurring after melting. A spectrofluorimeter

(PerkinElmer LS45) was used for luminescence measurements at excitation wavelengths of 360, 405 and 460 nm. Moreover, the excitation spectra of the samples were measured for emission wavelengths of 500 and 700 nm. The absorption spectrum of this sample is presented in Figure 2.7. The long wavelength band of the spectrum is assigned to ion Ce^{3+} [35, 49]. The short wavelength edge is mainly determined by the absorption of Ag^{+} that is formed by three bands with maxima at 219, 238 and 254 nm [50, 51]. From the spectrum is clear that there is negligible absorption at wavelengths beyond 350 nm. However, it was observed that if there is excitation at 355 nm linear photoionization of PTR glass is produced [52]. This means that the small absorption present at wavelength $>$ 350 nm is enough to contribute to ionization.

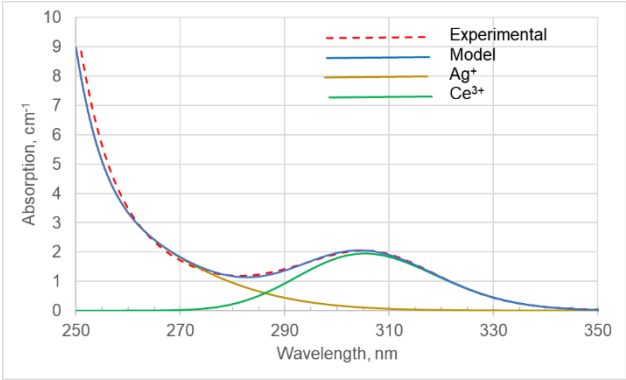

Figure 2-7 UV absorption spectrum of pristine PTR glass

To study this more in detail the emission spectrum of pristine sample was measured under excitation at 360 nm and is shown in Figure 2.8. The full emission spectrum was deconvolved into its Gaussian components to facilitate the analysis finding three main bands situated at 422, 505 and 582 nm. The formula used for modeling of Gaussian bands is the following.

$$A = \sum A_i \, exp\left[-ln2\left(\frac{N_i - N}{0.5\Delta_i}\right)^2\right] \tag{2-4}$$

Here, N (cm^{-1}) is wavenumber, N_i (cm^{-1}) is position for maximum, Δ_i = FWHM (cm^{-1}) and A_i is amplitude of band.

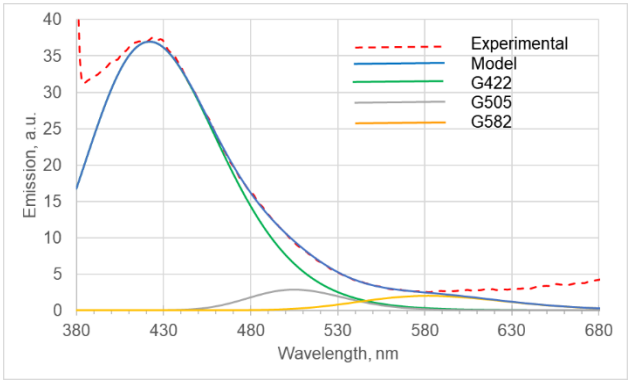

Figure 2-8 Luminescence spectrum of pristine PTR glass. Excitation – 360 nm

The main emission band is centered at 422 nm (Table 2.2) and includes a long wavelength tail that extends across the visible range, this is the cause of the blue luminescence shown in Figure 2.6. According to [5], luminescence band of Ce^{3+} has a maximum at 380 nm (blue luminescence) when excited in the vicinity of the absorption band with maximum at 305 nm. One supposition is that the emission band observed in Figure 2.8 with maximum at 422 nm is the luminescence of Ce^{3+}. The shift of this band to longer wavelengths could be the result of inhomogeneous broadening of luminescence and absorption spectra of Ce^{3+}. This happens when the excitation to lower energy levels of Ce^{3+} results in shifting the emission spectra to longer wavelengths.

Table 2-2 Parameters of emission and excitation bands of luminescence in pristine PTR glass

λ_{exc}, nm	Emission maxima, nm
360	422, 505, 582
405	390, 500, 690
460	390, 510, 587, 694, 760
λ_{em}, nm	Excitation maxima, nm
500	315, 375, 415, 443, 457
700	412, 442, 457, 472, 494, 518, 535, 551

In the same plot, two more emission bands in green and yellow regions can be distinguished with maxima at 505 and 582 nm. One of the suppositions is that these small bands could be connected with different Ag-containing centers. Such luminescent centers could be generated by partial chemical reduction of Ag during glass melting fabrication process or by ionizing radiation at 360 nm. To avoid parasitic signals from second order of monochromator used in spectrofluorimeter excitation wavelengths beyond 600 nm were not explored.

Figure 2.9 shows the emission spectrum of pristine glass under 405 nm excitation. The high intensity band is produced at wavelengths shorter than 430 nm and probably masked by the excitation beam signal (Table 2.2). This blue luminescence can be assigned to Ce^{3+} similar to that observed in Figure 2.8. However, this spectrum does not show any dip in the short wavelength part of the spectrum like in 360 nm excitation. In order to model the long wavelength tail of this band one has to consider that its maximum is centered at 390 nm and the width (FWHM) of two times wider than the one shown in Figure 2.8. The intensity of this emission band is decreased in about two times with respect to the band for excitation at 360 nm. Since absorption of Ce^{3+} at 405 nm never was observed one could suppose that the absorption causing the luminescence comes from energy transfer by centers with visible absorption to Ce^{3+} ion. To clarify this, additional studies are currently undergoing. The next band with maximum at 500 nm in the emission spectra can be found in both 360 and 405 nm excitation. This can be related to a silver containing center. Finally, a band with maximum at 690 was detected for the 405 nm excitation.

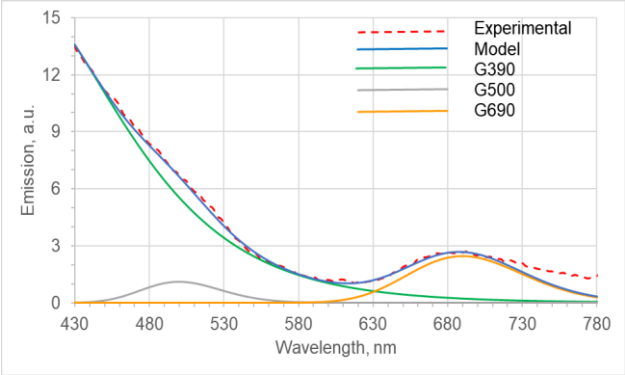

Figure 2-9 Luminescence spectrum of pristine PTR glass. Excitation – 405 nm

The next step was to explore the luminescence properties of pristine glass at longer excitation wavelength of 460 nm. The results are displayed in Figure 2.10. This spectrum still maintains a long wavelength tail of the UV band with modelled maximum at 390 nm. Moreover, the presence of this band that appeared in previous excitation wavelengths supports the supposition that this is the luminescence of Ce^{3+} and that results from the energy transfer of luminescent objects with visible absorption. Similar to the excitation at shorter wavelengths, the green luminescence band with maximum at 510 nm is still present. Similar to excitation at 360 nm, one can also find the yellowish low-intensity luminescence band centered at 587 nm. The most important feature for the 460 nm excitation wavelength is the appearing of two red luminescence bands at 694 nm similar to the spectrum in Figure 2.9 and a new one appearing at 760 nm.

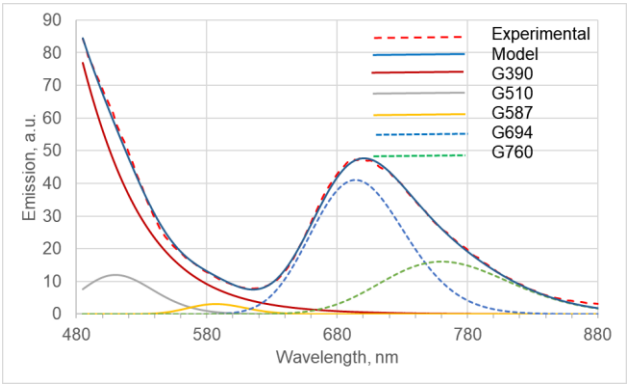

Figure 2-10 Luminescence spectrum of pristine PTR glass. Excitation – 460 nm

This means that excitation of pristine PTR glass from 360 to 460 nm results in the emission of several luminescence bands: Blue luminescence centered around 420 nm (long wavelength tail of high-intensity 390 nm band), green and yellow luminescence bands with maximum at 505 nm and 585 nm respectively, and two red luminescence bands with maxima at 690 and 760 nm that appear at longer excitation wavelengths. It should be noted that all these bands are broad and overlap each other and that there are no wavelengths where a single luminescence band could be excited.

The next step is to measure excitation spectra in main regions of emission spectra, green and red luminescence at 500 and 700 nm. One can retrieve from Figures 2.8, 2.9 and 2.10 that only blue (≈3/4) and green (≈1/4) luminescence contribute to 500 nm emission.

The excitation spectrum for 500 nm is presented in Figure 2.11. It shows a very pronounced increase of intensity at UV wavelengths close to 330 nm region. This part of spectrum could be produced by an efficient excitation of Ce^{3+} ion given the location of its absorption band that reached a maximum at 305 nm. It is important to notice that in the long wavelength region there are several excitation bands centered at 375, 415, 443, and 457 nm contributing to the green emission envelope. No absorption bands of this nature have been reported in pristine PTR glass before. However, UV exposed and thermally developed PTR glass shows absorption bands located at the same positions – 376 nm electron color centers, 412 nm atomic silver Ag^0, 455 nm complex band produced by different modifications of silver bromide Ag_nBr_m [53]. Assumptions could be made that these centers appear during the PTR glass fabrication process or are generated by parasitic UV irradiation coming from natural sources in the work environment.

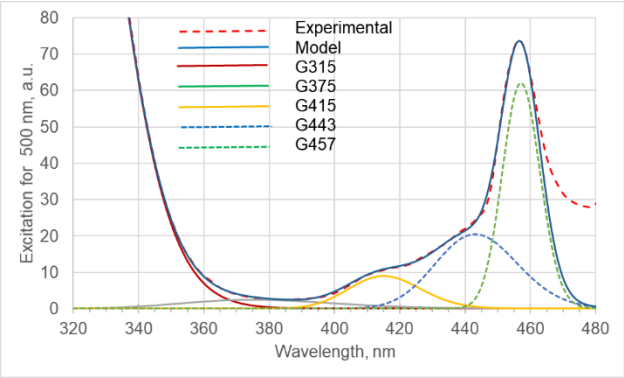

Figure 2-11 Excitation spectrum for emission at 500 nm in pristine PTR glass

Finally, the excitation spectrum for 700 nm was measured and is shown in Figure 2.12. It exhibits the same maxima as for emission fixed at 500 nm – 412, 442, and 457 nm. This could be connected with Ag^0 and Ag_nBr_m centers. Moreover, these spectra include a series of bands that continue up to the long wavelength region. No absorption bands were observed previously that could be associated with these excitation peaks. A supposition could be made that exponential long wavelength tail of Ag_nBr_m band [50] could include several different centers generating such bands. However, additional studies are required to verify this hypothesis.

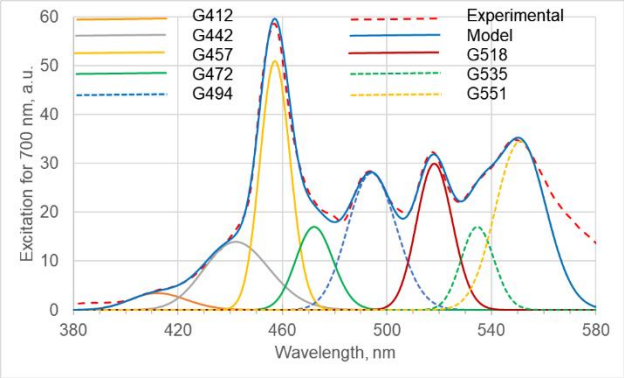

Figure 2-12 Excitation spectrum for emission at 700 nm in pristine PTR glass

Therefore one can conclude that the main species dominating the absorption in PTR glass at short wavelengths are Ag^+ and Ce^{3+}. It is proposed that long wavelength tail of Ce^{3+} could contribute to luminescence spectra of pristine glass. Long wavelength shifting of

luminescence can be produced by inhomogeneous broadening of absorption bands shown in Figure 2.7. Parameters of Table 2.2 demonstrate that there is luminescence effects including blue, green, yellow and red components in their emission spectra. The appearance of red luminescence becomes more significant for $\lambda > 400$ nm. Silver containing centers are supposed to be the cause of the luminescence observed in the green and yellow emission regions. The process of glass melting fabrication can be directly correlated to the generation of distinct types of luminescence centers. Non-irradiative energy transfer between Ce^{3+} and centers with visible absorption could provide an explanation for luminescence at excitation wavelengths in the visible region. Overlapping of emission bands is present in all measurements. It appears that PTR glass fabrication process and parasitic sources of UV irradiation can cause excitation peaks in the region similar to that of color centers and atomic silver. Luminescence centers of the form Ag_nBr_m could be present in different arrangements and their proper identification requires a complete study focused on this determination.

2.6 Effect of UV exposure and low temperature treatment on the luminescence properties of PTR glass

After the exploration of pristine PTR glass photoluminescence properties in previous section the next task was to study the effects on luminescence of UV photoionization and low temperature nucleation below T_g. A set of four samples (Glass ID: S21) were exposed to the same UV irradiation conditions of 0.9 J/cm^2 using a He-Cd laser at 325 nm to create exposed geometries of squared irradiated areas and linear stripes (a detailed description of the UV exposure system and irradiation procedure is provided in section 3.4). The UV exposed samples exhibited a greenish photoluminescence in the irradiated areas under a 405 nm excitation beam as shown in next Figure 2.7 (left). On the right side we show the luminescence

spectra of both pristine and UV exposed samples. If one compares, it is clear that in the luminescence spectra for the irradiated sample a band in the green region with maxima ~525 nm appears. This means that UV exposure definitely creates luminescent centers in the glass and this is the manifestation that some electronic processes already occurred.

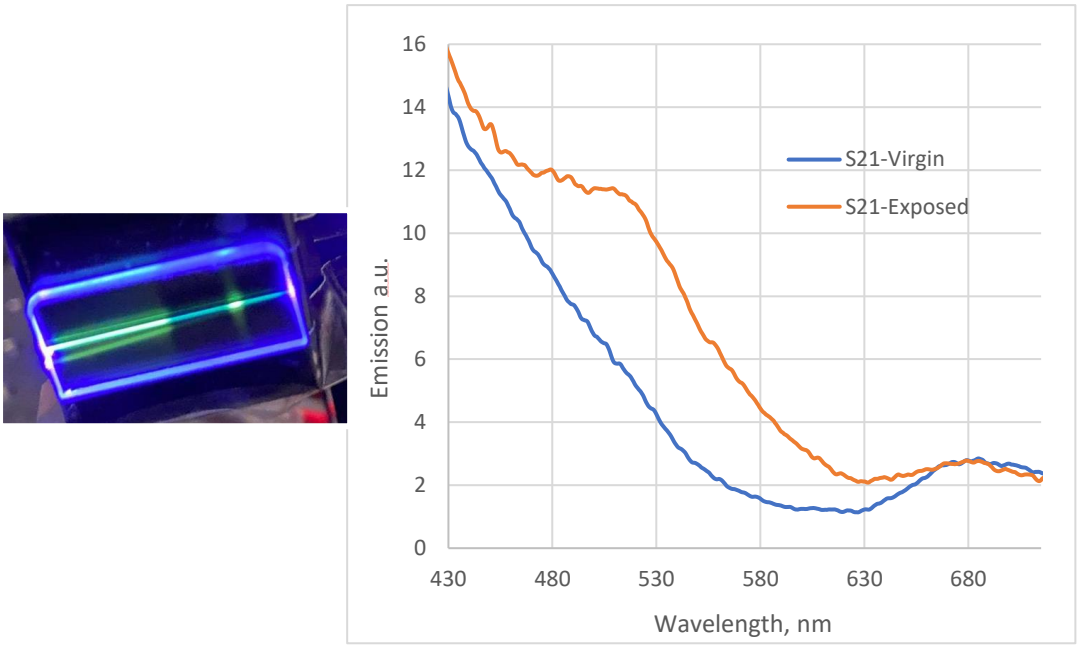

Figure 2-13 Photo of UV exposed sample (left) and emission spectra of pristine and UV exposed (S21) samples (right) under excitation of 405 nm laser beam

The absorption spectra of the UV irradiated samples also shows a difference in comparison with pristine glass, as a band related to color center generation [29] appeared in the vicinity of 376 nm as shown in Figure 2.8. Moreover, an absorption index increase in the short wavelength edge of spectra (~250 nm) indicates the photoionization of the Ce^{3+} ion being converted to Ce^{3++} that has an increased absorption in the UV region.

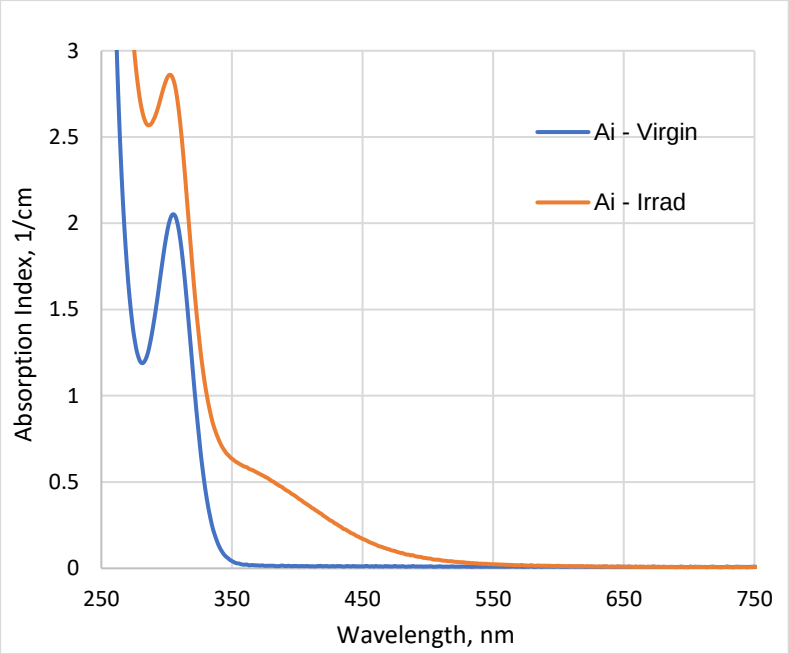

Figure 2-14 UV/VIS absorption spectra of pristine and UV exposed (S21) PTR glass samples

Now, as an attempt to explore the initial stage where phase transformations occur in the holographic recording process the four samples were thermally treated at temperatures of 300, 350, 400 and 450 °C using a conventional low temperature development furnace (see section 3.5). After thermal development the luminescence properties of the samples were explored collecting their emission spectra in a similar fashion as section 2.6 for excitation wavelengths of 360, 405 and 460 nm. First, the samples were measured impinging a probe beam from the side using a 405 nm laser diode in the same way the UV irradiated samples were measured previously. The observations for the thermally nucleated samples are presented in next Figure 2.9.

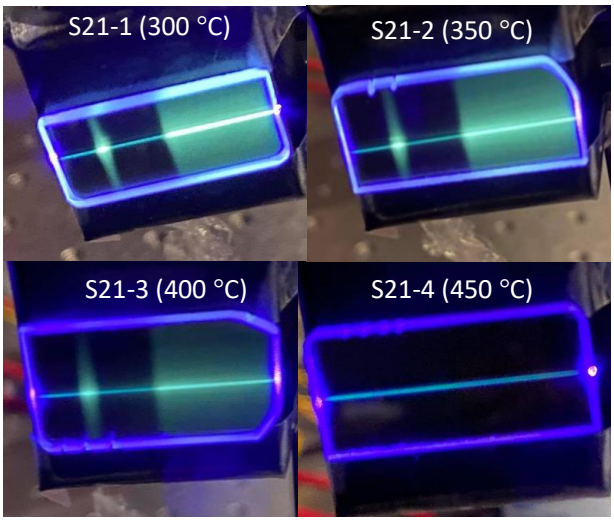

Figure 2-15 Photos of UV exposed and low temperature nucleated samples under excitation of 405 nm laser beam

As we can see, strong photoluminescence effects appeared in the squared and linear stripe areas exposed to UV for the samples nucleated at 300, 350 and 400 °C. The intensity of emission is the highest for the lowest aging temperature 300 °C and disappears for the 450 °C sample. It seems that as we increased the temperature of nucleation the luminescent centers are thermally bleached to reach a state of zero emission, where only the blue molecular scattering of the glass remains. Therefore it was confirmed that UV exposure and thermal treatment generates luminescent centers that appear for low temperatures and then disappear for high temperatures. Measurements via fluorescence spectrometer at 405 nm excitation wavelength revealed the following emission spectra of the developed samples, which correlates with the observations shown in Figure 2.9.

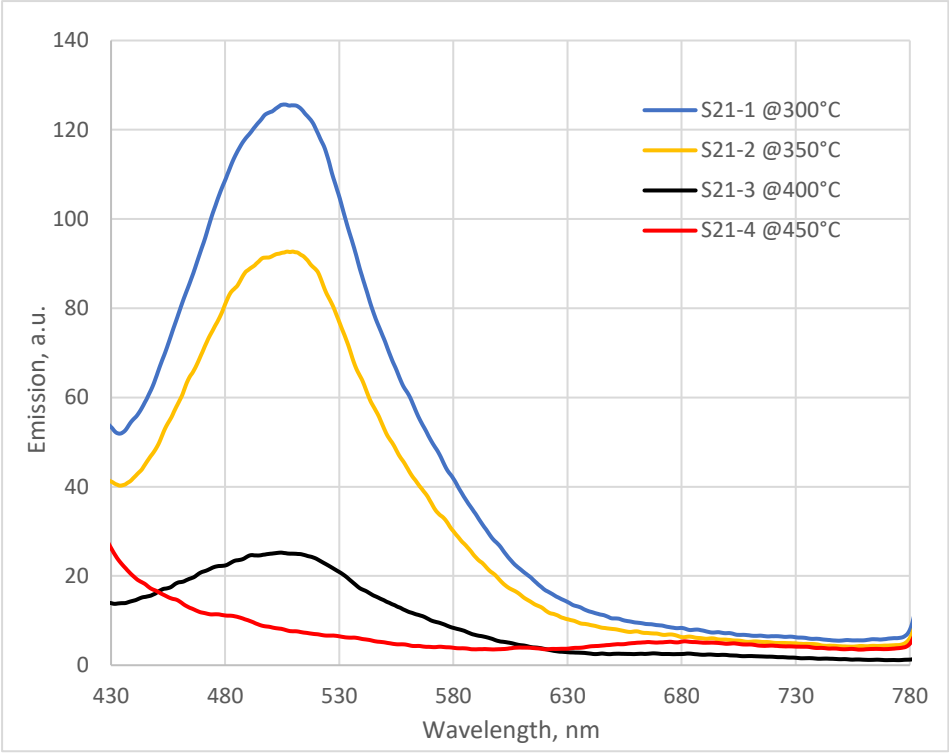

Figure 2-16 Emission spectra of UV exposed PTR glass samples nucleated at temperatures below T_g at 405 nm excitation

Once more we confirmed that at 405 nm excitation we detect an emission band that is highest for 300 °C and disappears for T > 400 °C. This band could be assigned to recombination of intrinsic color centers generated after UV exposure and silver containing particles that appear after thermal treatment. Optical absorption measurements in thermally treated samples showed that the band assigned to intrinsic color centers (~ 376 nm) decreases and another band in the vicinity 460 is created nm as we increase the temperature of nucleation (see Figure 2.10). The new band at 460 nm could be assigned to Ag-AgBr containing particles that are created as we increase the temperature of thermal treatment.

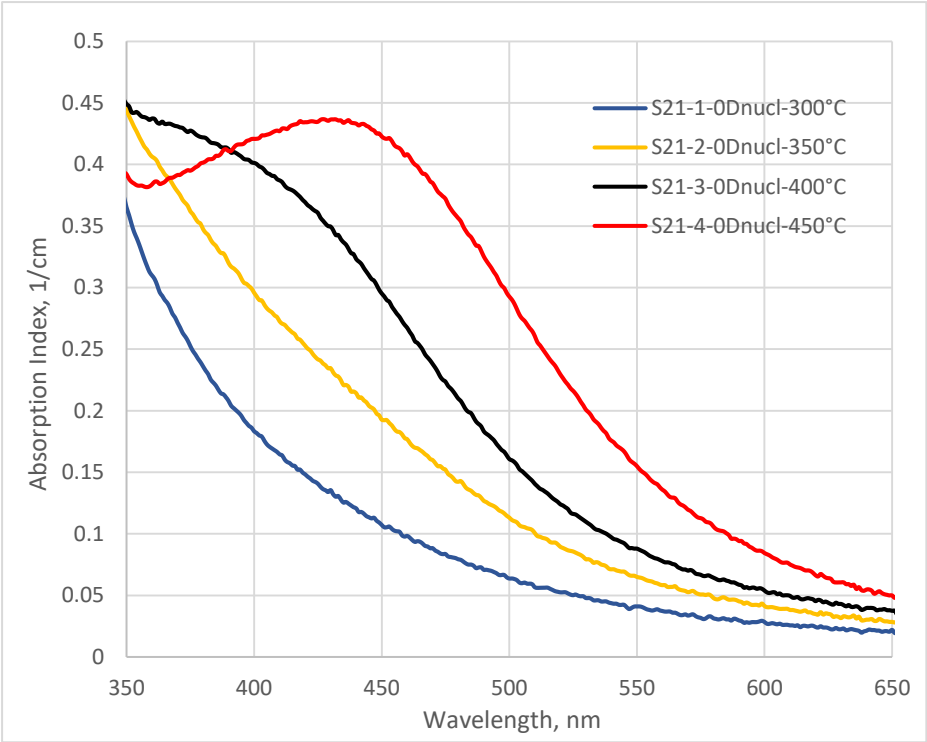

Figure 2-17 Absorption spectra of UV exposed PTR glass samples nucleated at temperatures below T_g

Therefore after analysis of absorption and luminescence spectra we have to conclude that changes in the atomic species after UV exposure and low temperature nucleation definitely occur. However, the scale at which these transformations occur cannot be inferred just with absorption and luminescence only, since these manifestations could include the contributions of scattering and reflection losses. Therefore, precise measurements of optical scattering become necessary for the complete study of phase transformations in PTR glass and this will be the main topic of study in the next Chapter 3.

CHAPTER 3: OPTICAL SCATTERING IN PTR GLASS

3.1 Introduction

One of the sources that introduce losses into holographic optical elements recorded in PTR glass is strong scattering produced by NaF nanocrystals that precipitate after UV exposure and thermal development. Nonetheless, very few information about experimental studies of optical scattering in PTR glass is reported. Despite the authors on [53] comment on the scattering properties of exposed and developed PTR glass, experimental data reported on those works was actually derived from attenuation (absorption plus scattering) calculations and no experimental tools for direct measurement of optical scattering were developed.

Therefore, to explore such an important property a high-sensitivity experimental setup for measuring scattering at 90° with respect to a 1-mm probe beam at 405 nm was constructed. The system provides 2D images of the far field intensity distribution of emission produced by the PTR glass samples when illuminated by the probe beam. This emission includes both scattering of probe radiation and luminescence excited by the probe beam. A narrowband filter at 405 nm was used to cut off luminescence. A high-resolution CCD captures the images and their scattering profile is converted into real values of scattering intensity through a specialized image processing software Image J. The system resolution is sufficient to detect the scattering level of highly homogeneous virgin PTR samples and represents a fundamental tool for the exploration of structural transformations that take place during the holographic recording process.

As mentioned in Chapter 2, the main goal of this dissertation is to detect the earliest stage at which structural inhomogeneities arise in the photo-thermo-refractive process required for hologram recording. To achieve this a specific algorithm of UV exposures and thermal

schedules below T_g has to be undertaken, and those along with all experimental procedures will be explained in detail in this Chapter 3.

3.2 Indirect measurements of scattering in PTR glass: Previous works

A detailed description of absorption and optical scattering spectra in PTR glass was presented in [53]. Where in order to retrieve the scattering spectrum of PTR glass, the losses of a pristine sample and the losses of the same sample after irradiation, thermal treatment and optical bleaching were subtracted. Therefore, the remaining losses caused mainly by scattering of glass were obtained and are presented in the spectrum of Figure 3.1.

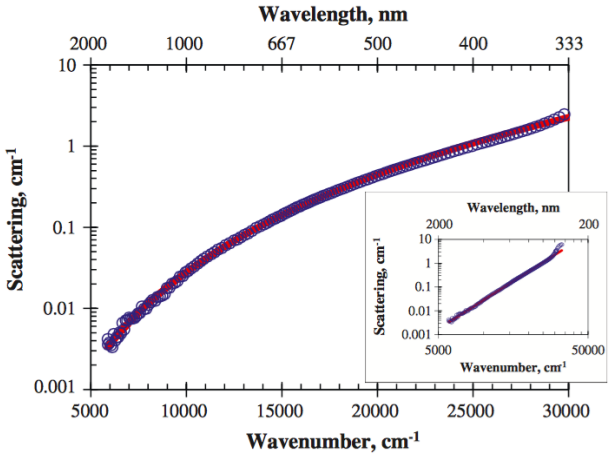

Figure 3-1 Induced scattering in PTR glass after UV exposure and thermal treatment [53]

It was shown in these works that absorption contributions of photoionized versions of Ce^{3+} that form after UV exposure are minimal in almost the entire spectrum except for the short wavelength range below 350 nm where more significant absorption of this type is present. An important equation presented in this paper is a function for spectral dependence of scattering or ($S_{th}(\sigma)$). This term can be expressed in the following form [53]:

$$S_{th}(\sigma) = S_0 \left(\frac{\sigma}{\sigma_0}\right)^N \quad (3\text{-}1)$$

Here the scattering coefficient at σ_0 is S_0 (in 1/cm), σ_0 is a constant and N is a real number that depends on the scattering nature of the glass. This study showed that the scattering in PTR glass that appears after the precipitation of a NaF crystalline phase follows the Rayleigh law of scattering. This conclusion was made based on information from Figure 3.1. It was measured from the logarithmic scattering plot that the trend corresponds to a straight line that in exponential form corresponds to a fourth power. Therefore, since $N = 4$ this confirmed that Rayleigh scattering is governing the process [54].

Moreover, it was observed in the same works that intensity of scattering is strongly dependent on the conditions of UV exposure and time of thermal treatment. Samples irradiated using different dosage levels and thermal treatment times were analyzed. Scattering coefficient versus dosage was plotted as isothermal lines at 515 °C for different thermal development times. One of the main key contributions of this work is that treating PTR glass for prolonged times caused the scattering to decrease with respect to dosage and vice versa for short thermal treatment times. Explanation of this opposite effect could be mathematically visualized through Rayleigh scattering equivalence of the form [53]:

$$S(N_p, r) \propto N_p r^6 \quad (3\text{-}2)$$

Here r is the crystal radius and N_p is the crystalline phase volume fraction. The inverse behavior exhibited in PTR glass for long and short development times versus level of dosage is mainly due to the competition of two effects. One effect is crystal size and the second is number of crystals (concentration). Moreover, it was shown in [53] that both effects could compensate each other as well resulting in a different combination of regimes that may allow for the mitigation of scattering in the process of hologram recording. The reality is that both effects are present in the process and contribute to the overall scattering level of the material.

Despite of above descriptions, it was not shown any direct measurements for the correlation between scattering intensity and photo-induced RIC of PTR glass.

3.3 Layout of the experimental setup

The experimental layout for direct measurements of optical scattering is shown in Figure 3.2. The setup includes a low power (mW level) laser diode emitting at 405 nm that is directed to a sample holder mounted on an XYZ translation stage using a set of mirrors. Through a couple of diaphragms, the diffraction of the beam is corrected and a slow focal length lens of f = 25 cm focuses the beam into the glass samples producing scattering. The probe beam enters the samples from one of the end facets and thanks to the slow divergence of the lens, the beam size remains almost constant throughout the sample volume. To mitigate the effect of parasitic surface scattering the end facet of the samples underwent fine polishing. Once scattering intensity is produced by the samples it is imaged onto a CMOS camera of 5.2×5.2 μm^2 pixel size placed at 90° with respect to the sample. To ensure that only the scattered light at 405 nm is measured a band pass filter is placed in contact to the camera filtering out all external light sources and the blue photoluminescence of the glass samples produced by the 405 nm beam. The camera is USB connected to a PC were digitalization of images is performed using Image J software. Further image processing allows to plot the 2D far-field scattering intensity profile of the samples and to convert it to numerical values across the sample length as it will be shown in the results section of the chapter.

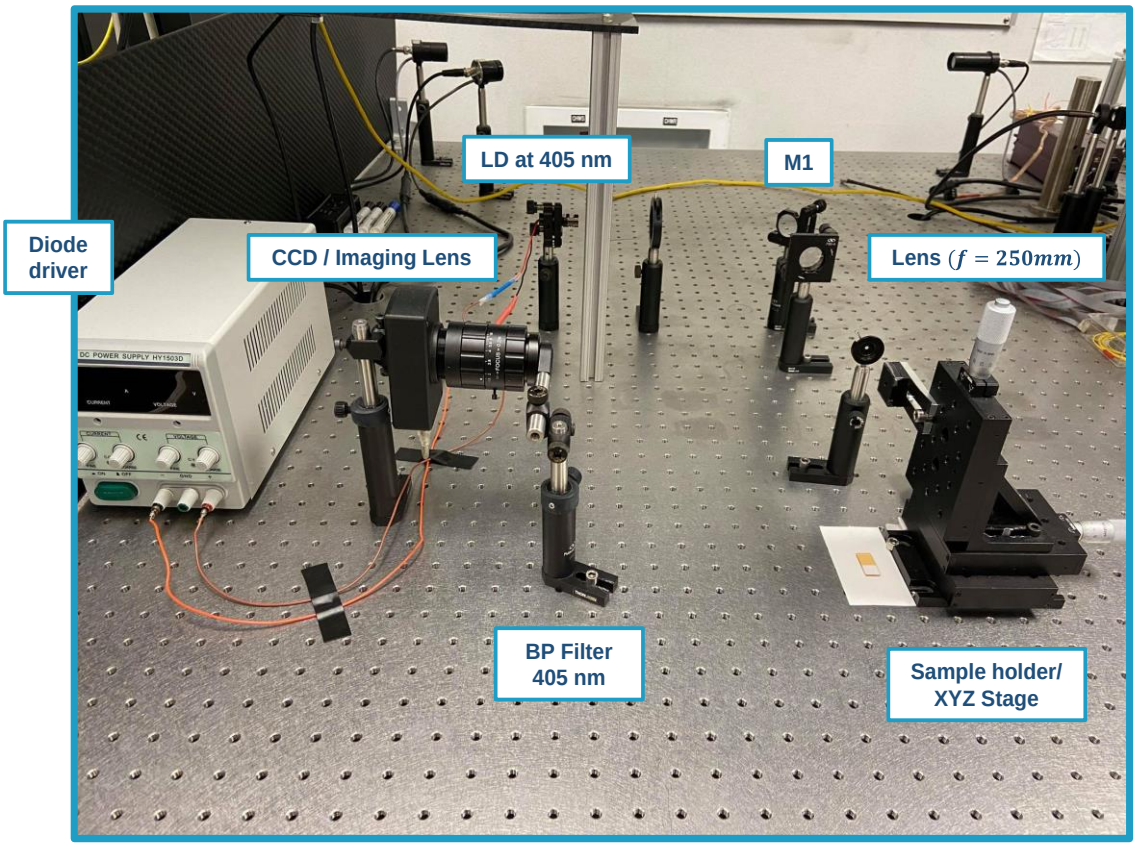

Figure 3-2 Experimental setup for measuring optical scattering at 90° relative to a probe beam at 405 nm

3.3.1 Sample preparation

Four 25×12.5×2 mm^3 samples of highly homogeneous PTR glass (Batch ID: S21) were prepared and polished. After preparation of samples, they were analyzed with a Fizeau interferometer to verify their optical homogeneity. Each of the samples was marked with a notch for their further identification in the experiments and the end-facets of the samples (where the probe beam enters and exits) were polished to mitigate parasitic scattering as much as possible. It is known that virgin PTR glass samples are a single-phase material that exhibits low scattering of optical radiation. This value is usually around 1.5-2.0 times higher than the value found for fused silica. Therefore, to account for a reference value of scattering an additional sample of non-photosensitive glass (Batch ID: V24) with dimensions

$25\times12.5\times2$ mm^3 was prepared. The reference sample V24 (commercial PTR glass) accounts for a level of scattering 1.75 times higher than that for fused silica. With this sample, we will be able to compare any scattering measurements to the scattering level of high-purity fused silica.

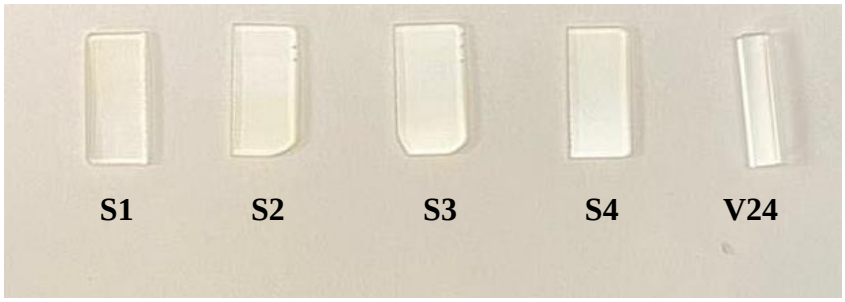

Figure 3-3 PTR and V24 glass samples prepared for scattering measurements

3.3.2 Measurements of scattering on virgin samples

The virgin PTR glass and reference samples were mounted onto the sample holder of the scattering setup for initial measurements. Afterwards, the probe beam was incident into the samples using a power level of 10.5 mW. The far field scattering intensity perpendicularly produced throughout the volume of each sample was captured with the procedure explained before. Finally, the non-photosensitive V24 glass sample was measured for standardization of reference level compared to fused silica. Photos of the 2D scattering profiles of the samples are shown in Figure 3.4 with respective sample IDs.

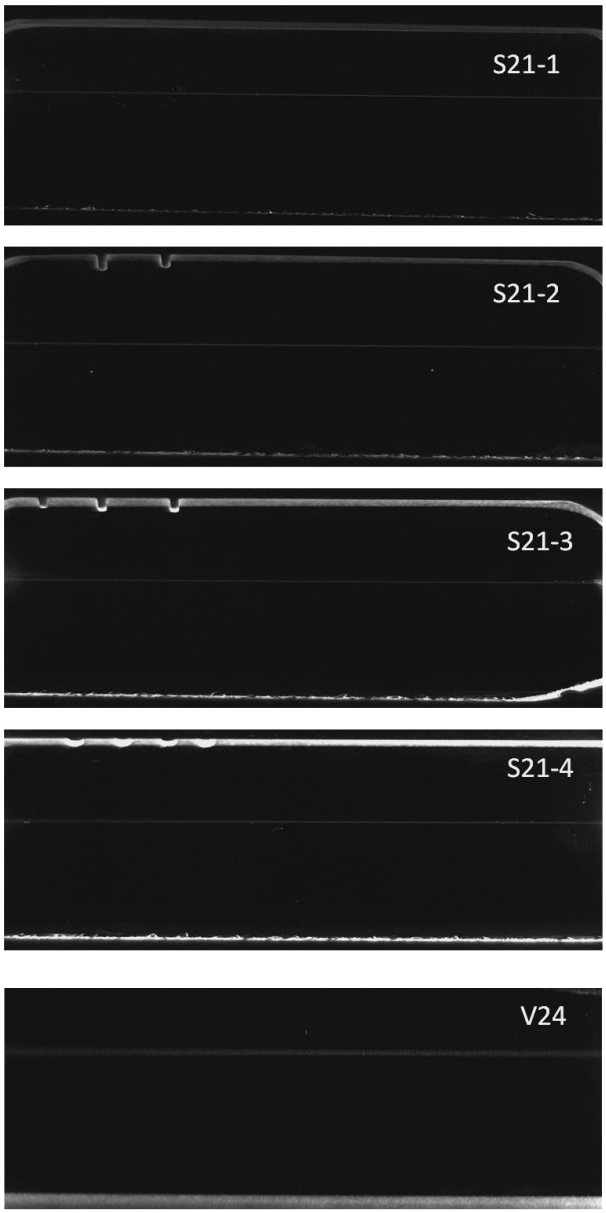

Figure 3-4 Photos of virgin PTR glass and V24 samples taken with high-resolution CCD camera showing scattering of 405 nm laser beam (Glass ID: S21)

As we can observe, the sensitivity of the system is capable of detecting the scattering produced by virgin samples at 405 nm. Moreover, one can notice from the photos that level of scattering for all them at this stage seems to be nearly the same. Furthermore, by means of Image J software one is capable to digitalize the 2D scattering photos and retrieve plots of scattering intensity values versus distance across the sample as we show in Figure 3.5.

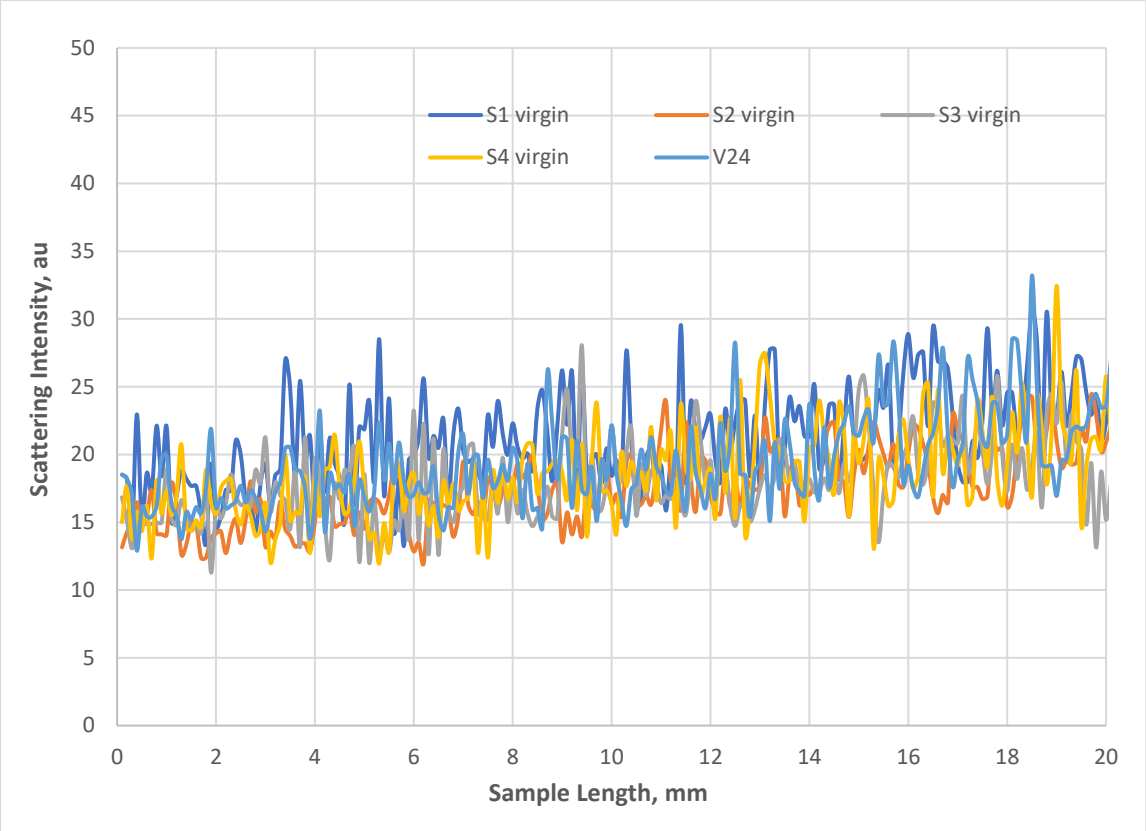

Figure 3-5 Scattering intensity versus distance along probe beam propagation in the PTR (virgin) and V24 glass samples

Digitalization of images confirms that the scattering level of the virgin samples is in average the same for all of them within the noise level. This result is expected as they belong to the same type of glass batch S21 and the samples were prepared and measured under the same laboratory conditions. These results mean that both PTR and V24 glasses exhibit a scattering level 17±5 a.u. (1.5-2.0 times fused silica units).

3.4 UV exposure system for recording of square and stripe geometries

Now, the next step of the project involved to analyze the scattering properties of the samples after irradiation in the photosensitive band of the material (280 nm – 350 nm). To achieve this, a 325 nm He-Cd laser (Kimmon IK3501R-G) of 30 mW optical power was used. The laser beam was directed to a sample holder using a couple of mirrors while a motorized

translation stage controlled by LabVIEW interface scanned the samples across the beam. By moving the sample in the x direction, Gaussian stripes of 1 mm thickness were produced. On the other hand, consecutive scans in the x and y direction we will create a uniform square pattern as shown in Figure 3.6. Flat exposures (or squares) will allow characterization of scattering in uniformly irradiation patterns, whereas Gaussian stripes will be used for accurate measurements of RIC with a liquid cell shearing interferometer [22].

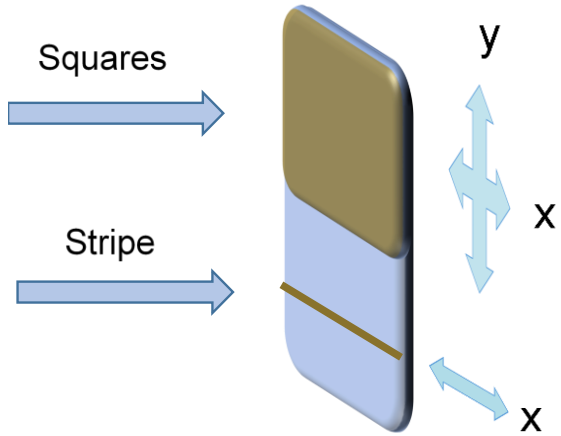

Figure 3-6 Illustration of recorded geometries on the volume of the (S21) PTR glass samples. Squares (top) and Gaussian stripes (bottom)

To provide a precise dosage of 0.9 J/cm^2 to the 10×10 mm^2 squares and 1-mm thick Gaussian stripes the laser beam at 325 nm was scanned across the samples with a constant speed V in the horizontal direction given by [22]:

$$V = \sqrt{\frac{2}{\pi}}\left(\frac{P}{\omega D_{max}}\right) \tag{3-3}$$

Where P is the total power of the laser beam, ω is the half-width of the beam at the level of 1/e^2 and D_{max} is the maximal dosage at the center of the stripe that in this case was the prescribed value of 0.9 J/cm^2. After UV exposure, each of the samples was analyzed again under the scattering setup obtaining the following results.

3.4.1 Measurements of scattering after irradiation

After exposure to 325 nm UV laser the samples were re-measured at the scattering setup. We observed that the samples exhibited a slight enhancement of scattering of a few scattering intensity units after UV irradiation. However, the increment in scattering was observed throughout the entire volume of the sample and not only in the irradiated areas. There is an assumption that the atomic refractive index of the glass may increase after UV irradiation causing increased scattering due to a local change in the atomic volume. However, just strong green luminescence appeared after illumination with the 405 nm beam in both square and stripe geometries. In previous works, we have explained that this luminescence may be due to distinct silver aggregates generated in the glass or color centers that appear after UV exposure. The high-resolution CCD captured the scattering images after UV irradiation and its corresponding digitalization plots are shown in next Figure 3.7.

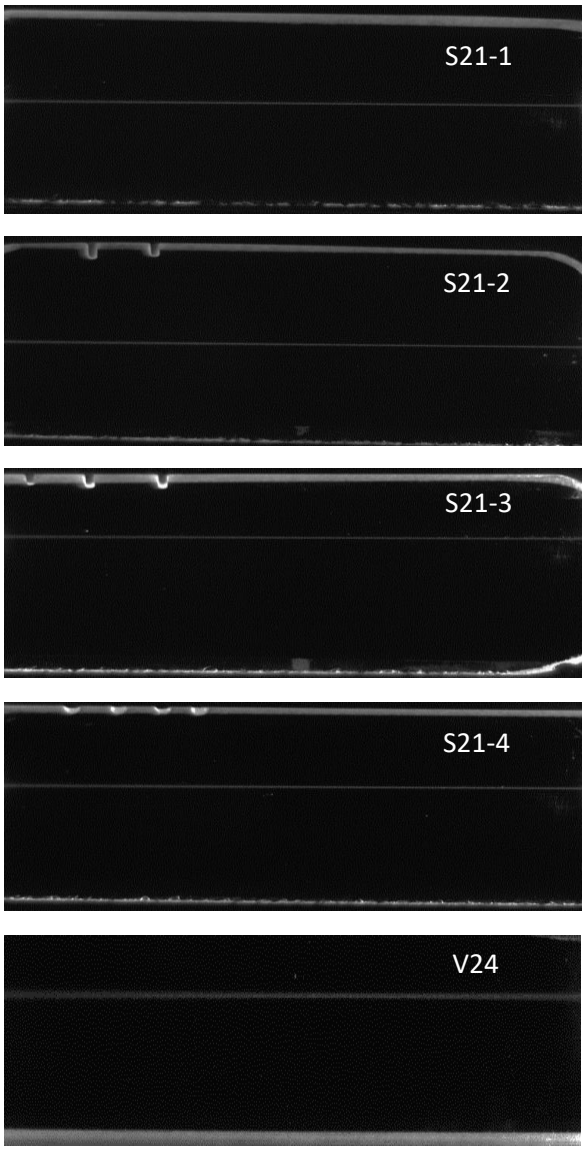

Figure 3-7 Photos of irradiated PTR glass and V24 samples taken with high-resolution CCD camera showing scattering of 405 nm laser beam (Glass ID: S21)

Once again, one can notice from the photos that level of scattering for all them at this stage seems to be the same. Digitalization confirms that the level of scattering was not increased within the accuracy of measurements (19±5 a.u.).

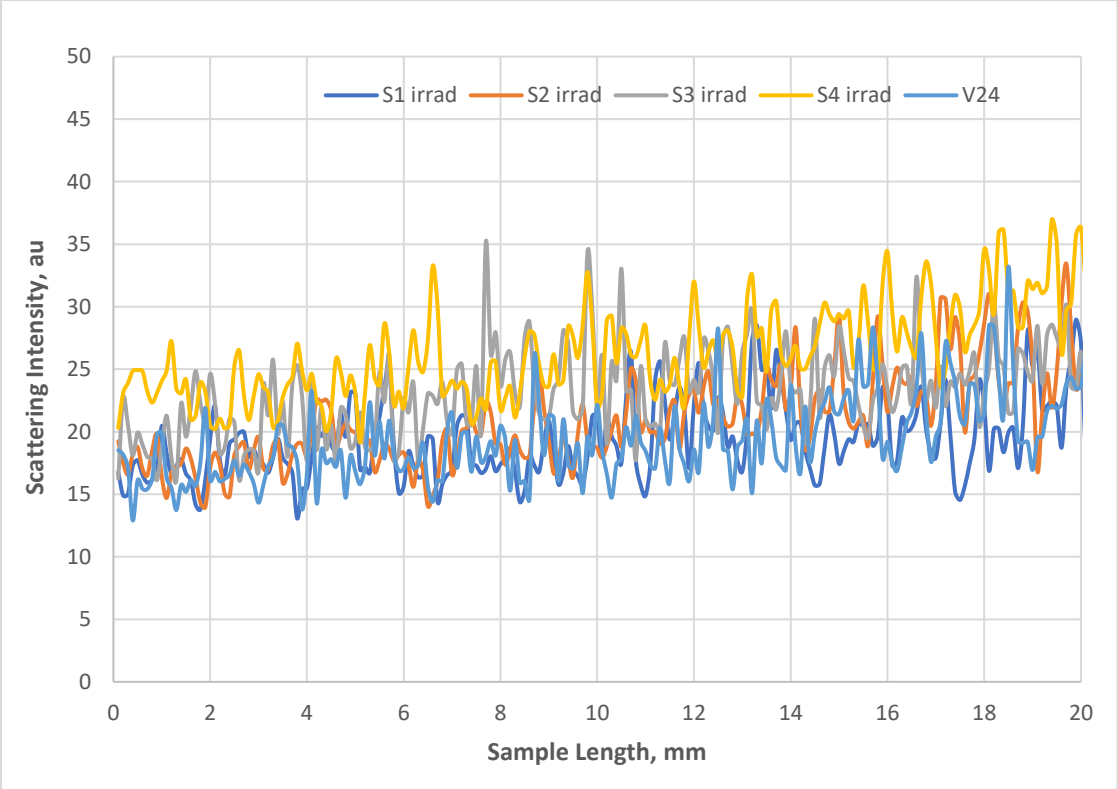

Figure 3-8 Digitalization of scattering intensity versus distance along the PTR (irradiated) and V24 glass samples

3.5 Thermal regimes below T_g

As the main goal of this project is to explore phase transformations in PTR glass after UV exposure and thermal treatment a specific algorithm of thermal schedules was developed. We know that structural transformations in PTR glass start in the vicinity of T_g, which is usually situated around 470 °C. Therefore, the nucleation regimes were chosen at temperatures lower than T_g as an attempt to detect the lowest temperature at which structural homogeneities could be generated in the photo-thermo-refractive process necessary for hologram recording. All samples underwent thermal treatment in a 1.8 kW Lindberg/Blue development furnace using the thermal regimes presented in Table 3.1. All the samples were subsequently cooled down to room temperature after development for their further analysis in the scattering setup.

Table 3-1 Sample IDs and respective thermal conditions provided in the experiment

Sample ID	Thermal regime
S21 - 1	300 °C for 85 min.
S21 - 2	350 °C for 85 min.
S21 - 3	400 °C for 85 min.
S21 - 4	450 °C for 85 min.

3.5.1 Measurements of scattering after low temperature nucleation

The PTR glass samples under study were analyzed at the scattering setup after thermal treatment with the main goal of detecting the appearance of structural inhomogeneities. Again, we use an optical power of 10.5 mW at the incident beam on the samples and cut off luminescence from samples using band pass filter. The 2D scattering profiles of the samples after their respective thermal-development regimes along with cellphone photos with no filter are presented in next Figure 3.9.

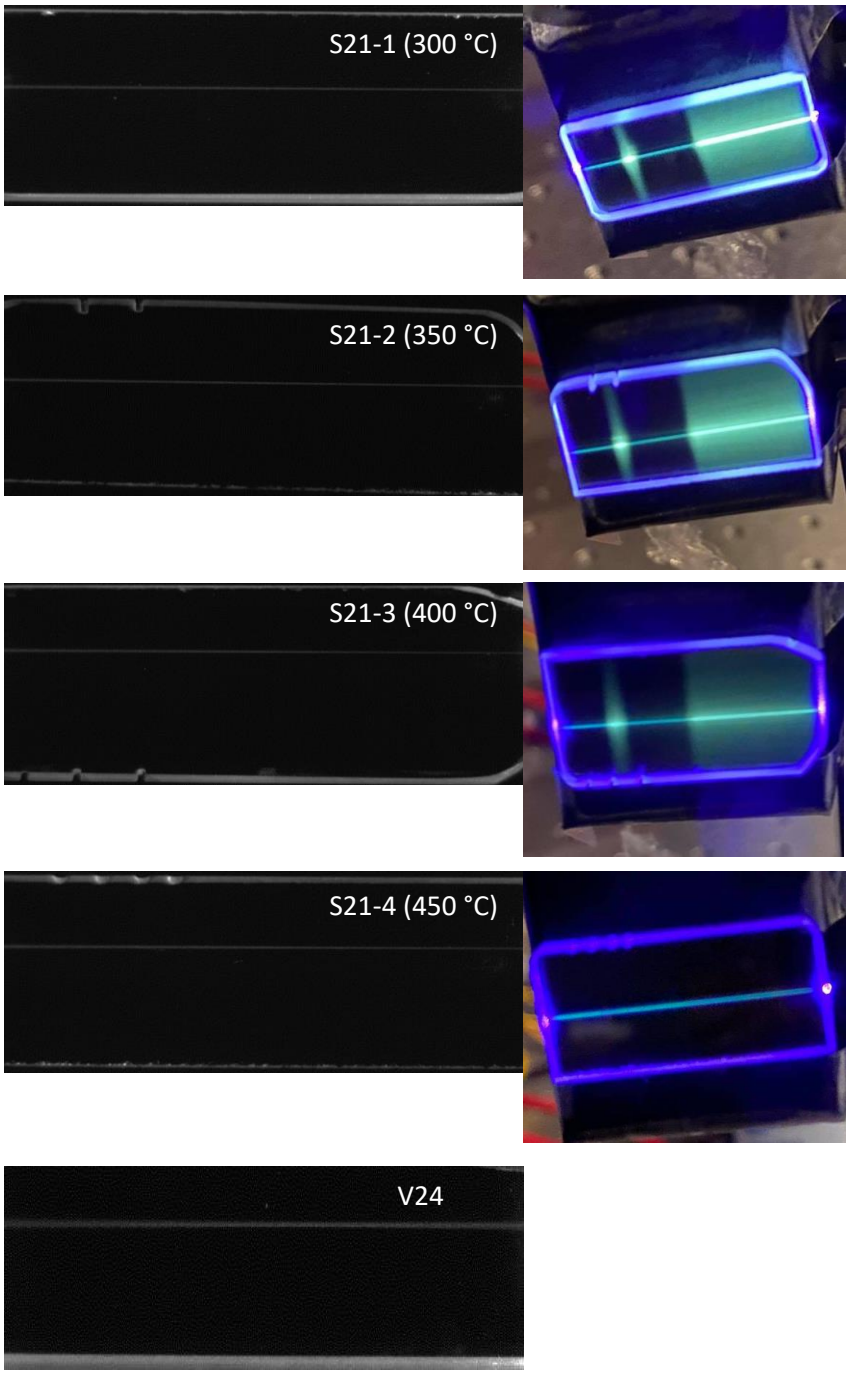

Figure 3-9 Photos of thermally developed PTR glass and V24 samples taken with high-resolution CCD camera showing scattering of 405 nm laser beam (Glass ID: S21) (left). Photos of the samples under excitation at 405 nm laser beam taken with camera (right)

First, we can observe from the scattering setup photos (left of Figure 3.9) that the level of scattering seems to be very similar for all the samples. On the other hand, photos taken with no filter reveal that a mix of scattering and luminescence is present even when samples are developed at temperatures way below the T_g of the glass, at 300°C. One can notice that the

luminescence intensity decreases as we increased the temperature of thermal treatment. Thermal bleaching of color centers at higher temperatures may be the cause of this effect. Digitalization of plots shows that the scattering level of the samples at 405 nm is the same as for pristine and irradiated samples (17±5 a.u.) and, contrary to luminescence, it is not possible to detect clear a step-like increase in the square and stripe geometries for thermal developments at these low temperatures as we see for T > 500°C.

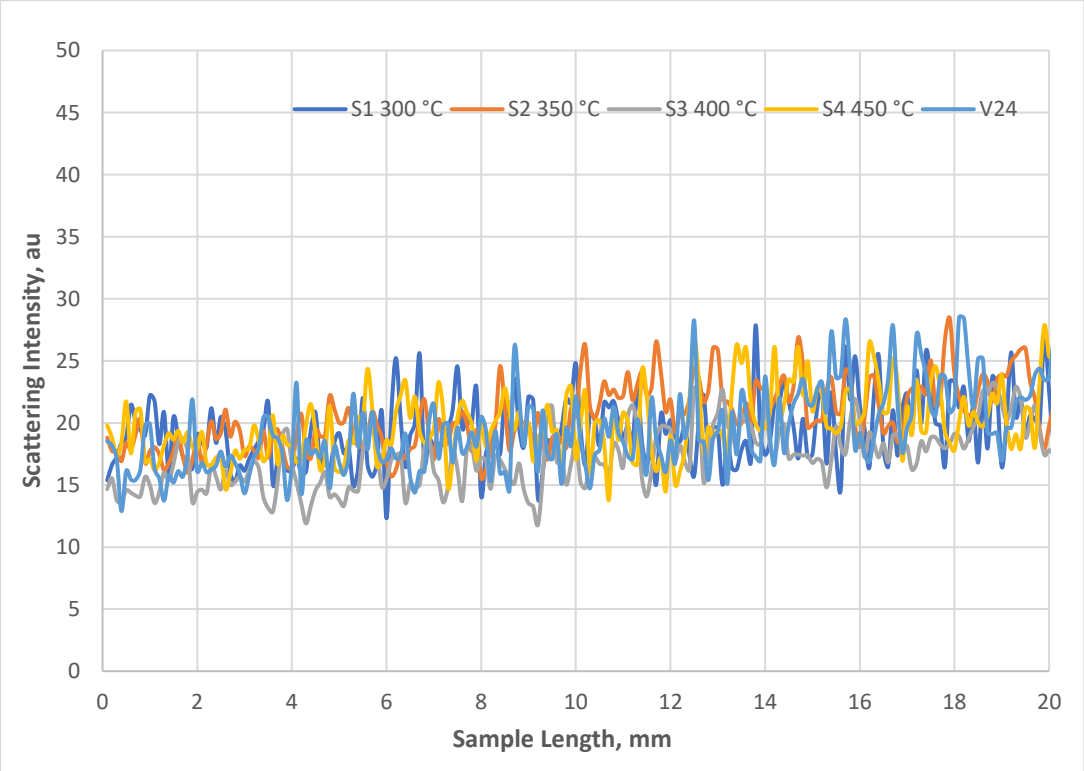

Figure 3-10 Scattering intensity versus distance along the PTR (nucleated) and V24 glass samples

These results are a significant advancement in our understanding of structural inhomogeneities generated in PTR glass at temperatures lower than T_g. We can state that the transformations observed on the previous luminescence chapter occur at atomic scales only since the constructed system has proved detection of NaF nanocrystals of about 80 nm size for samples developed above T_g. No step-like increments of scattering in PTR glass occurred after heat treatments up to 450^{o}C.

CHAPTER 4: LOW TEMPERATURE ION EXCHANGE METHOD IN PTR GLASS

4.1 Introduction

As one of the main holographic materials employed for high power laser applications and robust laser systems exposed to harsh environments, there has been special interest in the enhancement of chemical durability and laser damage threshold of PTR glasses. It is known that both properties are intimately related to the structuring of surface layers of the material, where micro-cracks appear during the polishing process of glass sample preparation. On the other hand, on top of surface imperfections there is an inevitable deposition of organic compounds contained in the atmosphere that introduce additional light absorption and decreasing the laser threshold. For this reason, there is a necessity to develop methods to improve the surface characteristics of glass without changing the intrinsic properties of the holographic element like its diffraction efficiency, spectral selectivity, etc. One of the methods that has proven reliability in the enhancement of the glass surface properties is the so-called ion exchange method. In this Chapter 4, we will describe the theoretical basis of this method and present an experimental layout capable of performing low-temperature ion exchange (Na^+-K^+) in the surface of PTR glass samples. Moreover, we will present initial results of a system that provides measurements of surface refractive index called "waveguide method" (or inverted Abbe). This system will be used to characterize the waveguides generated on the surface of PTR glass samples treated with the ion-exchange method. By measuring conditions of total internal reflection or "coupling angles", we will retrieve information of effective mode indices that will be in turn introduced to the WKB method to calculate their refractive index profiles.

4.2 The ion exchange method: theoretical basis

One of the process used to increase the strength of a glass media is the ion exchange method or commonly known as 'chemical tempering'. Such method can be found in multiple industrial processes including the fabrication of glass bottles, in vehicle windows and other applications [55]. To perform ion exchange, a pristine glass sample is immersed into a high purity salt bath (about 99% purity) at temperatures lower than T_g; then, while the sample is in the bath the alkali ions in the liquid salt and at the surface of glass are exchanged in an inter-diffusion process as shown in Figure 4.1 [56].

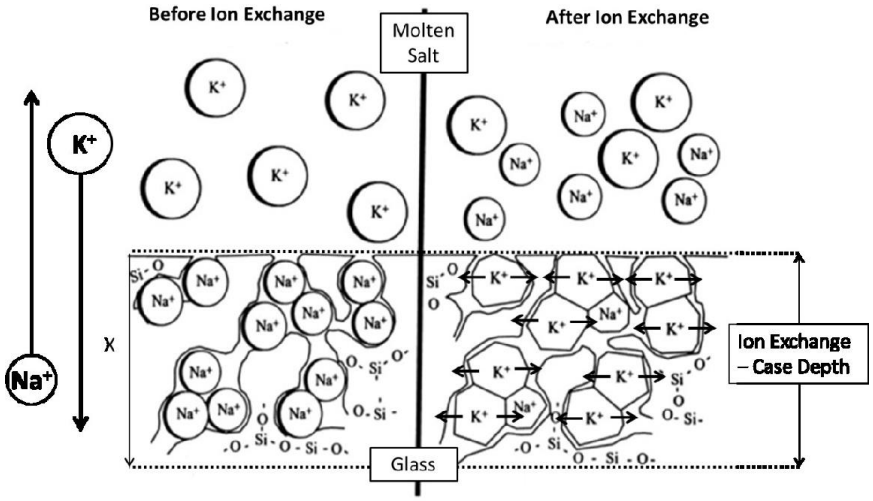

Figure 4-1 Representation of an ion exchange process showing the inter-diffusion of Na^+ and K^+ ions in the glass surface [56]

The exchange triggered by thermal energy produces increased strength that comes from the fact that ions adding to the glass surface account for larger ionic radius than released (original) ones. Therefore, the process of ionic site replacement generates a layer of strong compressions in the surface of the glass. The depth of penetration of the ion exchange layer has been measured to be in the order of tens of micrometers and depends on temperature of diffusion and immersion time as shown in [57].

On the other hand, the inner layers of the sample located at the interface between original glass and ion-exchanged one will experience tensile stresses that will compensate the compressive ones as shown in Figure 4.2.

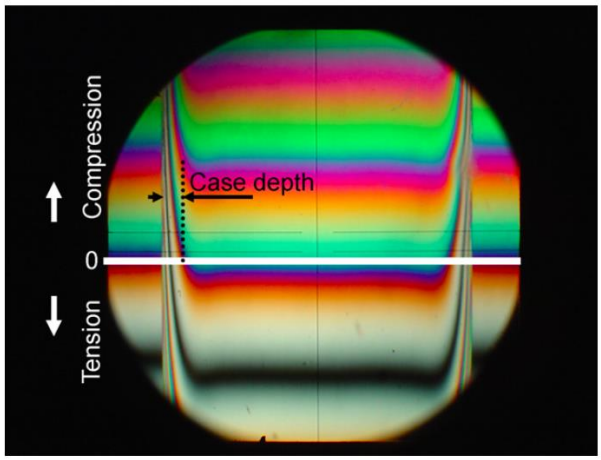

Figure 4-2 Stress pattern in a sample treated by the ion exchange process. Image taken in a polariscope supplied with a Babinet compensator [55]

The authors of [55] showed that in the process of ion exchange the original glass network formed by SiO_2 bonds remains almost unaltered. In this way, the transmission properties of the material remain the same as that from the initial glass and no iridescence is present. Let us suppose that Na^+ ions of a soda-lime silicate glass will be exchanged by K^+ ions from a molten salt in an ion exchange process. Also, that the thickness of the glass sample is greater than the penetration depth for several orders of magnitude. As K^+ ions are heavier than Na^+ ones, the total mass of the sample is expected to increase linearly as the concentration of K^+ in the sample goes up. Then, the rate of exchange $C(x,t)$ will be described by a differential equation of the form [55]:

$$\frac{\partial C}{\partial t} = \frac{D_K}{1-\alpha C}\left[\frac{\partial^2 C}{\partial x^2} + \frac{\alpha}{1-\alpha C}\left(\frac{\partial C}{\partial x}\right)^2\right] \tag{4-1}$$

$$\alpha = 1 - \frac{D_K}{D_{Na}} \tag{4-2}$$

Where t is immersion time, x is a position coordinate that represents depth of penetration and D_K or D_{Na} are self-diffusion coefficients of sodium and potassium. At $t = 0$

the exchange rate can be written as $C(x,0) = 0$; whereas the boundary conditions of the system can be denoted by $C(0,t) = 1$ and $C(\infty,t) = 0$. However, this can be considered just as a simplified model of the inter-diffusion process and a more meticulous analysis will be required to increase precision [58]. One of the consequences of the ion exchange process is the residual stress accumulated in the glass, which can be measured in the transverse profile of a treated sample. One way to achieve this is using mechanisms where the birefringence is measured [59]. A simple approach to evaluate the birefringence effects includes the use of a polariscope and a Babinet compensator as shown in [55]; if a sample is illuminated parallel to its facets, it will be distinguished a pattern of fringes that reflects the transverse stress profile as shown in Figure 4.2.

Some other factors that could contribute to residual stresses at the surface of the glass are thermal effects generated during the heating of ion exchange process and cracks generated in the sample preparation [60]. As explained in Section 4.1 of this dissertation, besides the enhancement of the glass properties through the ion exchange method the fabrication of planar waveguides in PTR glass is another main goal of the investigation. Therefore, it is fundamental to include in the analysis the determination of the refractive index profile close to the surfaces of the sample. It has been found [55] that for regular soda-lime silicate glasses the refractive index reaches a maximum for the edges (compressive zones) and decreases monotonically as we go deeper into the inner parts of the sample. This was confirmed by optical measurements where both TE and TM polarized waves were coupled into the surface of a sample using a double prism [55, 59]. In these refractometry studies two different index profiles were obtained (one for each polarization), the Δn experienced between TE and TM waves is due to the birefringence caused by the residual internal stresses of the sample. In Figure 4.3, we can observe an example of this effect in a soda-lime silicate glass plotted versus distance from the surface. The demonstration of these results on soda-lime silicate glasses will be of main

importance in our further development and characterization of planar optical waveguides in PTR glasses.

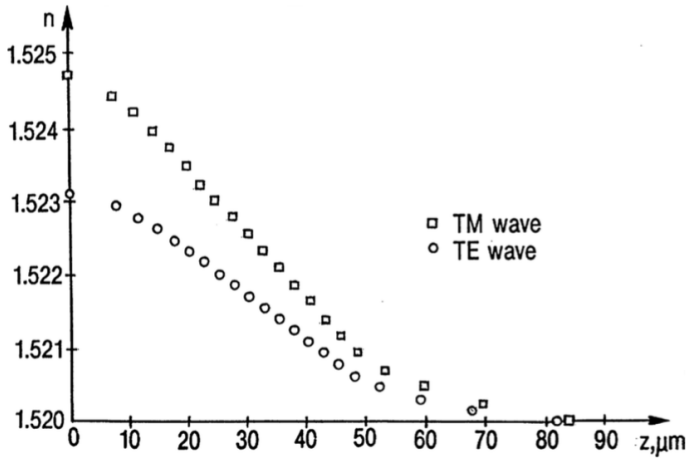

Figure 4-3 Example of refractive index profiles as a function of sample depth in soda-lime-silicate glass exposed to ion exchange treatment for TE and TM polarized light [55]

An important remark is that for low temperature ion exchange treatment using species with large difference in ionic radii but similar atomic refractions (e.g. Na^+-K^+), the source of refractive index increment is compressive stresses in the waveguide layers of the sample. Whereas for ion exchange processes between ions with similar atomic radius (e.g. Na^+-Ag^+), refractive index increase is mainly caused by difference in atomic refraction of silver and host glass and birefringence will considerably decrease in the optical waveguide [61].

4.3 Low temperature ion exchange method in PTR glasses

Besides the enhancement of glass surface properties, there is a necessity for the development of planar optical waveguides on PTR glass. Such waveguides might be used for integrated optics and other applications [62]. However, when it comes to PTR glasses there are only a few investigations that show a detailed description of the performance of low temperature ion exchange method for waveguide fabrication [63]. In such work, it was

demonstrated the feasibility of planar optical waveguide fabrication using the exchange of Na^+ ions from the original glass with Ag^+, K^+, Rb^+ and Cs^+ dissolved in different salt melts. Similar to soda-lime silicate glasses an increase in the refractive index from the surface was observed as a result of the exchange process. The refractive index profiles for the proposed waveguides were calculated using the inverse WKB method [64]. However, the aforementioned studies were conducted in a Chlorine version of PTR glass and this dissertation investigates PTR glasses of a slightly different composition.

4.4 Experimental layout for low temperature ion exchange in PTR glass

An experimental setup to perform low temperature ion exchange in PTR glass samples was prepared. A low temperature furnace (Thermolyne 62700) was used to heat up the samples to the prescribed thermal regimes. To maintain as low as possible the concentration of impurities that may hinder the diffusion process, both platinum crucible and platinum sample holder were used. Furthermore, a 99% purity KNO_3 salt was selected for the exchange process of Na^+ for K^+ ions. Figure 4.4 shows a photo of the experimental setup built at CREOL laboratories.

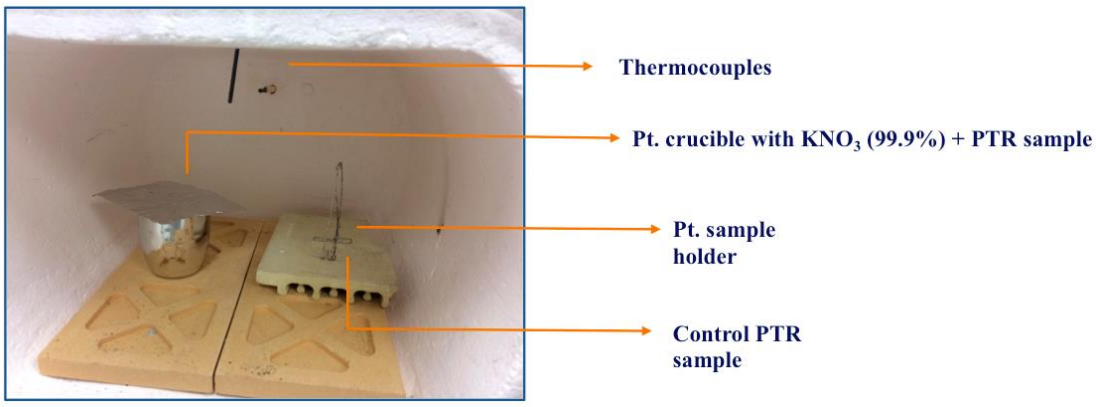

Figure 4-4 Experimental layout for low temperature ion exchange in PTR glass

The control sample introduced in the experiment is a virgin PTR glass sample that will not be involved in the diffusion process. However, it will allow for tracking any refractive index changes produced solely by the heating process. As the goal of the experiment is to perform low temperature ion exchange, the maximum diffusion temperature was chosen to be about 80 °C below T_g. Ion exchange experiments were carried out at temperatures of 365 °C and 400 °C, and times of 60 minutes and 180 minutes. The full thermal regime applied in the process comprises several steps of heating, as shown in Figure 4.5.

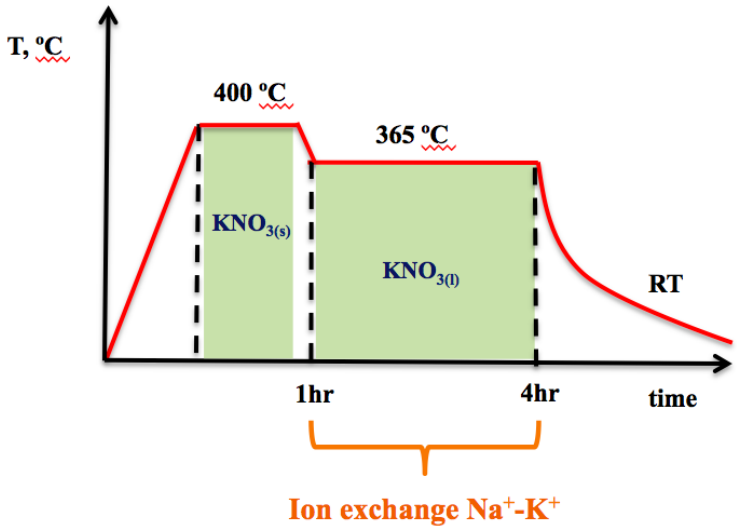

Figure 4-5 Thermal regime for the ion exchange in PTR glass samples

First, the 100 mL platinum crucible is loaded with KNO_3 salt to about half of its volume and consequently heated up to 410 °C until the salt melts. Second, the temperature is ramped down to the prescribed ion exchange conditions and remains constant throughout the entire process. When it reaches room temperature, the sample is taken out from the salt bath and the salt batch returns to its solid-state condition and both platinum holder and sample are rinsed with distilled water at low pressure. This will help to eliminate any excess of KNO_3 crystals that agglomerated due to surface tension. At first glance, the physical appearance of a PTR

glass sample does not seem to change after the ion exchange process. However, further characterization discussed in next sections will show that the actual surface layers of the glass were modified.

4.5 Inverted Abbe method for measurements of surface refractive index

As explained in previous sections of this Chapter, one of the expected features resulting from the ion exchange process is an increase in the surface refractive index of the samples. Therefore, the next part of the investigation comprises an experimental setup that uses the waveguide method (or inverted Abbe) [65] for measurements of refractive index in a substrate using a coupling prism.

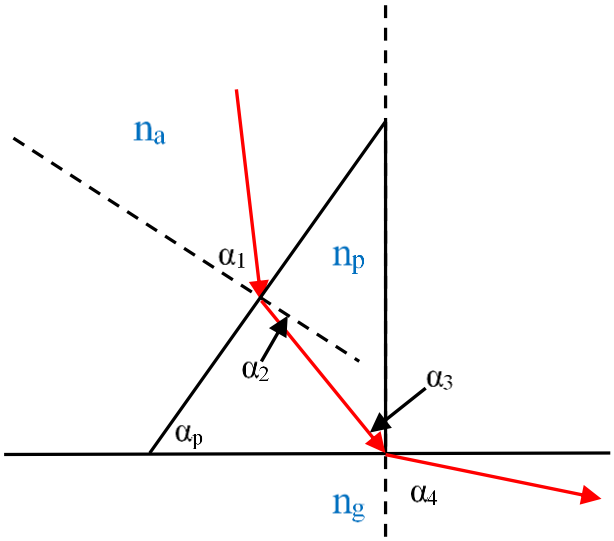

Figure 4-6 Ray tracing for surface refractive index measurements using a right corner prism. n_a, n_p, and n_g are refractive indices of air, prism and glass respectively. α_p, α_i are angle at prism base and incident and refracted rays respectively

The proposed method was applied to conduct measurements of incident angle α_1 for a condition of total internal reflection when the angle at the base of the prism is $\alpha_4 = 90°$ like depicted in Figure 4.6. Then, through geometrical ray analysis one can obtain an expression

for the refractive index of the glass surface. First, applying Snell's law at the interface between the coupling prism and the glass substrate we can find:

$$n_g = n_p sin\alpha_3 \tag{4-3}$$

Where n_g represents index of glass substrate ($n_g = 1.4990$ for virgin PTR glass) and n_p is index of the prism ($n_p = 1.965$ for $\lambda = 633$ nm). It can be inferred by trigonometry as well that α_3 is the summation of the apex angle of the prism α_p plus α_2; hence one can use:

$$\alpha_3 = \alpha_p + \alpha_2 \tag{4-4}$$

Is important to mention that α_1 and α_2 in Figure 4.6 are negative and considering that refractive index of air is $n_a = 1$. Applying Snell's law one more time at the interface between air and prism we get:

$$\alpha_2 = Arcsin\left(\frac{sin\alpha_1}{n_p}\right) \tag{4-5}$$

If we substitute (4-5) into (4-4) and then to (4-3) we arrive to the following expression for the index of the glass:

$$n_g = n_p sin\left(\alpha_p + arcsin\left(\frac{sin\alpha_1}{n_p}\right)\right) \tag{4-6}$$

The starting point for the measurements involves normal incidence to the prism $-\alpha_1 = 0$ using a linearly polarized He-Ne laser operating at 633nm. A set of mirrors and a diaphragm are used to suppress diffraction while the sample under study is pressed to the base of the coupling prism using a set of screws in the back of a customized holder (Figure 4.7). To achieve efficient optical contact between the high index prism and the sample, matching index liquid has to be applied. Finally, the holder is mounted onto a rotary stage to enable angular measurements of total internal reflection condition. The beam refracted inside the glass sample produces a light spot on the end facet of the sample. In case of a sample with a uniform refractive index (n_g), an increase of an incident angle at the coupling prism (α_1) would result in increase of an angle of refraction inside the sample (α_4). Therefore, the bright spot in the

end face would move towards the front of the surface of the sample. When an angle of total internal reflection is achieved ($\alpha_4 = 90°$), the refracted beam propagates along the front surface of the sample (surface wave) and its refractive index can be calculated using (4-6).

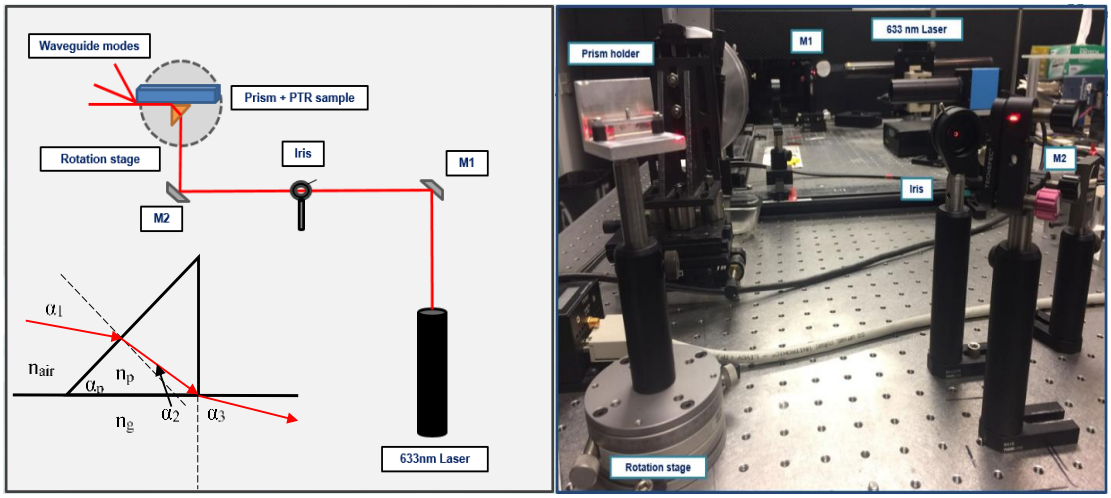

Figure 4-7 Experimental setup for a waveguide method (inverted Abbe) of refractive index measurement: an optical scheme (left) and a photo of a real setup (right)

4.6 Experimental evidence of ion exchange in PTR glass: Planar waveguides

One of the first evidences indicating that the ion exchange process modified the surface layers of PTR glass was the appearance of a "bright layer" observed on both sides of the treated samples under Abbe refractometer. As shown in work [63] for the refractive index profile of K^+ exchanged waveguides, an increase of about 10,000 ppm is estimated after the treatment. The calculation of such gradient refractive index profiles is based on the experimental determination of individual propagation constants of waveguide modes [65].

$$\tilde{N}_m = c/\upsilon_m \tag{4-7}$$

Where c is the speed of light in vacuum and υ_m is the phase velocity of a specific mode m. Therefore, an effective way to selectively excite waveguide modes in the ion-exchanged region becomes necessary and the use of the inverted Abbe method described in Section 4.5 can be one of the solutions. It should be noted that if an ion exchange layer has a refractive

index increment and thickness that enables waveguiding, strong light coupling in the surface of the sample would be observed for several incident angles α_1 that correspond to efficient excitation of waveguide modes. To prove this concept, a sample of PTR glass (Glass ID: N95) that underwent ion exchange (T = 400 °C, t = 60 min) was tested under the waveguide method observing the excitation of three modes (m = 3). Subsequently, incident angles at the coupling prism (α_1) were measured for each excited mode and effective refractive indices were calculated using equation (4-6). In Table 4.1, we present incident angles at the coupling prism (α_1) with their corresponding value of n_g for sample N95.

Table 4-1 Incident angles and calculated refractive index for N95 sample

α_1 (deg)	n_g
9.90 (m=1)	1.5057
9.50 (m=2)	1.5012
9.10 (m=3)	1.4967

It is worth noticing that sample N95 was treated under ion exchange process several months before this measurement; this means that the ion exchange layer can withstand standard environmental conditions for long periods without being easily destroyed. Moreover, to ensure repeatability of the experiments three more samples treated with different ion exchange conditions were tested under the inverted Abbe method for effective refractive index characterization. The sample's ID and provided ion exchange regimes are presented in the Table 4.2.

Table 4-2 Sample ID and ion exchange conditions for refractive index measurements

Sample ID	Ion exchange regime
VC60-E	T = 365 °C ; t = 180 min
NR2-IE-1	T = 400 °C ; t = 60 min
NR2-IE-2	T = 365 °C ; t = 180 min

Results of incident angles and corresponding refractive indices for the new set of samples are presented in Tables 4.3 to 4.5. As we can see, refractive indices of excited modes are very close to known values of refractive index for PTR glass. This indicates that the waveguide method has capability to be used as a reliable characterization tool for the fabrication of planar optical waveguides. Furthermore, comparison of refractive index between the highest and lowest order modes shows an increment of the same order to the one estimated in [63] for K^+ waveguides.

Table 4-3 Incident angles and calculated refractive index for VC60-E sample

α_1 (deg)	n_g
9.05 (m=1)	1.4962
8.90 (m=2)	1.4945
8.75 (m=3)	1.4928
8.65 (m=4)	1.4917

Table 4-4 Incident angles and calculated refractive index for NR2-IE-1 sample

α_1 (deg)	n_g
9.30 (m=1)	1.4990
9.00 (m=2)	1.4956
8.90 (m=3)	1.4945
8.60 (m=4)	1.4911

Table 4-5 Incident angles and calculated refractive index for NR2-IE-2 sample

α_1 (deg)	n_g
9.00 (m=1)	1.4956
8.70 (m=2)	1.4922
8.40 (m=3)	1.4889
8.30 (m=4)	1.4877

4.7 Calculation of refractive index profiles of the ion-exchanged waveguides using the inverse WKB method

One of the questions that arises after the experimental determination of mode indices demonstrated in previous section is: what is the refractive index profile $n(z)$ (where z is the direction of diffusion) of the ion-exchanged waveguides? How to calculate it? Therefore, there is a necessity for a method that enables the calculation of these profiles. One of the preferable methods for solving such monolithically decreasing functions is the inverse Wentzel-Kramers-Brillouin approximation [63, 66]. The WKB method is based on the determination of the propagation depth for each mode taking as starting point the modal equation. Therefore, based on the previous works from White and Heidrich [64] we will provide a simplified algorithm that will allow us to use the experimentally calculated mode indices from the inverted Abbe method and feed them into the WKB approximation for the calculation of a refractive index profile $n(z)$.

4.7.1 Mathematical algorithm

First, if we assume a lossless electromagnetic field that travels in the x plane of a waveguide with coordinate z being normal to the surface of the sample, a transverse electric (TE) mode can be described with the following equation [64].

$$E_y = F(z)exp[i(k_x x - \omega t)] \tag{4-8}$$

As we know, the above solution holds for different mode eigenvalues that will be reduced in the WKB approximation by applying the boundary conditions at the surface of the waveguide and transforming the solution into:

$$\int_0^{z_m}[n^2(z)-n_m^2]^{1/2}dz=\frac{4m-1}{8},m=1,2,\dots,M \tag{4-9}$$

Now, to find the z_m values (depth point) derived from the n_m values (mode indices) and thus arrive to an approximation of $n(z)$, it is needed to re-define equation (4-9) as a summation of integrals as follows [64]:

$$\sum_{k=1}^{m}\int_{z_{k-1}}^{z_k}[n^2(z)-n_m^2]^{1/2}dz=\frac{4m-1}{8} \tag{4-10}$$

Then, we suppose that $n(z)$ will be a segmented linear equivalency that links the experimental values of n_m, for example:

$$n(z)\approx n_k+\frac{(n_{k-1}-n_k)}{(z_k-z_{k-1})}(z_k-z)\forall z_{k-1}\le z\le z_k \tag{4-11}$$

If a mid-point value replaces the factor $n(z)+n_m$ within the specific extent of z from equation (4-11). The solution for z_m (depth point) becomes:

$$z_m=z_{m-1}+\left[\left(\frac{3}{2}\right)\left(\frac{n_{m-1}+3n_m}{2}\right)^{-1/2}(n_{m-1}-n_m)^{-1/2}\right]\left\{\left(\frac{4m-1}{8}\right)-\frac{2}{3}\sum_{k=1}^{m-1}\left(\frac{n_{k-1}+n_k}{2}+n_m\right)^{1/2}\left(\frac{z_k-z_{k-1}}{n_{k-1}-n_k}\right)\times\left[(n_{k-1}-n_m)^{3/2}-(n_k-n_m)^{3/2}\right]\right\}\forall m=2,3,\dots,M, \tag{4-12}$$

$$z_1=\frac{9}{16}\left(\frac{n_0+3n_1}{2}\right)^{-1/2}(n_0-n_1)^{-1/2} \tag{4-13}$$

Usually, the surface index of the sample n_0 is an unknown parameter. For this reason, we have to select an arbitrary numerical procedure to find the best approximation for n_0 and one is to take the value of n_0 that yields the profile with the smoothest curve. In other words, we have to find the value of n_0 that reduces the following expression to the minimum [64]:

$$\sum_{k=0}^{M-2}\left[\frac{\frac{n_{k+2}-n_{k+1}}{z_{k+2}-z_{k+1}}-\frac{n_{k+1}-n_k}{z_{k+1}-z_k}}{\frac{z_{k+2}+z_{k+1}}{2}-\frac{z_{k+1}+z_k}{2}}\right]^2 \tag{4-14}$$

Other very important boundary conditions to take in account for the method are:

$$n(z_m)=n_m \tag{4-15}$$

$$z_0=0 \tag{4-16}$$

$$n_0=n(0)=n(z_0=0) \tag{4-17}$$

Following this mathematical algorithm, now we have a way to calculate values of z_m with the use of equation (4-12) just by obtaining z_1 from equation (4-13) and feeding the

experimentally calculated values of mode indices n_m. Thus, by simply plotting the values of n_m vs z_m a refractive index profile $n(z)$ will be obtained. To show an example of how the inverse WKB method can be applied, let us take the experimentally determined mode indices n_m presented in Table 4.1 of section 4.6 for a sample treated under ion-exchange process and calculate z_1. By applying the described algorithm, we obtain the values of z_m shown in next Table 4.6.

Table 4-6 Values of n_m vs z_m obtained through the WKB method

$n_0 = 1.510$ (surface index, arbitrarily selected as first good approximation)	$z_0 = 0$
$n_1 = 1.5057$	$z_1 = 4.9471$
$n_2 = 1.5012$	$z_2 = 6.2523$
$n_3 = 1.4967$	$z_3 = 9.960$

By plotting these pair of data and fitting them to a monotonically decreasing function starting at the surface ($z = 0$) we obtain the refractive index profile $n(z)$ of the ion exchanged waveguide integrated on sample N-95.

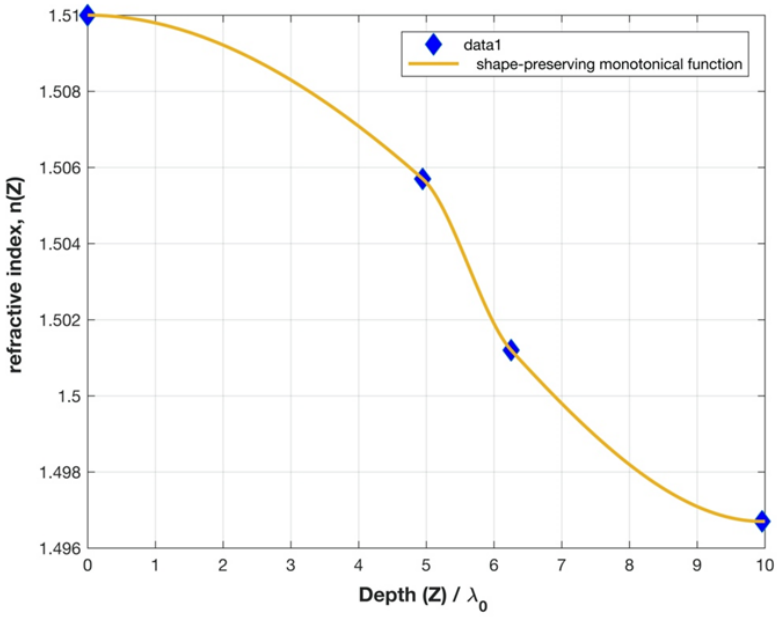

Figure 4-8 Refractive index profile of an ion-exchange waveguide integrated on PTR glass sample N-95 obtained through the inverse WKB approximation

As we can see from the plot in Figure 4.8, $n(z)$ is divided by λ_0 as a factor of normalization to the free-space wavelength. As this operation simplify the calculations and does not alter the outcomes, factors of λ_0 have been excluded from the mathematical derivation of this procedure [64]. This means that according to the inverse WKB approximation the depth (z) of this waveguide will be of about 7 μm given that we excite the modes using a linearly polarized He-Ne laser operating at 633 nm. This value is within the range for planar optical waveguides on a glass substrate with an air cladding.

CHAPTER 5: CONCLUSIONS

The UV absorption spectrum of PTR glass matrix is formed by an exponential tail of intrinsic absorption at wavelengths shorter 220 nm and a wide asymmetric band with maximum at 232 nm that is assigned to Fe^{3+} impurity. Full composition PTR glass shows short wavelength absorption edge formed by Ag^{+} and Ce^{4+}. No absorption bands were detected in visible spectral range.

Photoluminescence in PTR glass matrix at excitation shorter 300 nm show a combination of photoluminescence of intrinsic L-centers and Fe^{3+}. No luminescence (at available level of sensitivity) was observed at excitation longer 300 nm.

Photoluminescence of full composition PTR glass at excitation wavelengths of 360, 405 and 460 nm was studied. Emission in blue, green and red regions was detected. For 360 nm excitation, the maxima of detected bands are at 422, 505 and 582 nm. For 405 nm excitation, maxima are at 500 and 690 nm. For 460 nm excitation, maxima are at 510, 587, 694 and 760 nm.

The excitation spectra for emission at 500 nm show bands with maxima at 315, 375, 415, 443, and 457 nm. The excitation spectra for emission at 700 nm were found at 412, 442, 457, 472, 494, 518, 535 and 551 nm.

The mechanism of short wavelength luminescence excited at 360 nm is direct excitation of long wavelength tail of Ce^{3+} absorption band with maximum at 305 nm. The origin of short wavelength luminescence for excitation in visible is not clear and requires additional study. Visible luminescence is assigned to low concentration silver aggregates mainly Ag^{0} and Ag_nBr_m produced during glass fabrication process.

UV exposure of PTR glass results in generation of a broad absorption band at 376 nm assigned to intrinsic color centers. Excitation of the exposed glass to 405 nm results in bright

green luminescence with maximum at 515 nm that could be assigned to excitation of color centers.

Low temperature treatment up to 450°C shows bleaching of the color center band and growth of the band at 460 nm. This band could be ascribed to Ag-AgBr containing particles. Initial heating to 300°C causes increase of the green luminescence. Further temperature rise results in decrease of its intensity and complete disappearing after heating at 450°C.

The scattering measurements showed that no structural changes of large scales occurred after heat treatments of PTR glass up to 450°C. We conclude that structural transformations resulted in additional absorption and luminescence occur at atomic scale. Large scale structural transformations in UV exposed PTR glass occur only after heating above 450°C that is comparable to T_g for this glass.

The multimode planar waveguides were created by low temperature ion exchange $K_{melt} \leftrightarrow Na_{glass}$ at 360°C. Effective refractive indices of waveguide modes were measured and refractive index profiles were calculated. This results pave a way to creation of holograms in planar waveguides.

REFERENCES

1. D S.D. Stookey, “Photosensitive glass – A new photographic medium,” Industrial and Engineering Chemistry 41, 856-861 (1949).

2. D V.A. Borgman, L.B. Glebov, N.V. Nikonorov, G.T. Petrovskii, V.V. Savvin, A.D. Tsvetkov. Photothermal refractive effect in silicate glasses. *Sov. Phys. Dokl*., 34, No 11 (1989) 1011-1013.

3. D. Gabor, A new microscopic principle, Nature, 161, 777 (1948).

4. L.B. Glebov, N.V. Nikonorov, E.I. Panysheva, G.T. Petrovskii, V.V. Savvin, I.V. Tunimanova, V.A. Tsekhomskii. Polychromatic glasses - a new material for recording volume phase holograms. Sov. Phys. Dokl., 35, No 10 (1990) 878-880.

5. Glebov, Leonid B. "Volume holographic elements in a photo-thermo-refractive glass." Journal of Holography and Speckle5.1 (2009): 77-84.

6. Dubrovin, V. D., Ignatiev, A. I., & Nikonorov, N. V. (2016). Chloride photo-thermo-refractive glasses. Optical Materials Express, 6(5), 1701-1713.

7. O.M. Efimov, L.B. Glebov, L.N. Glebova, K.C. Richardson, and V.I. Smirnov, “High-efficiency Bragg gratings in photothermorefractive glass,” Applied Optics **38**, 619-627 (1999).

8. Sevian, A., Andrusyak, O., Ciapurin, I., Smirnov, V., Venus, G., & Glebov, L. (2008). Efficient power scaling of laser radiation by spectral beam combining. Optics letters, 33(4), 384-386.

9. Andrusyak, O., Smirnov, V., Venus, G., Rotar, V., & Glebov, L. (2009). Spectral combining and coherent coupling of lasers by volume Bragg gratings. IEEE journal of selected topics in quantum electronics, 15(2), 344-353.

10. Glebov, L. B., Smirnov, V. I., Stickley, C. M., & Ciapurin, I. V. (2002, June). New approach to robust optics for HEL systems. In *Laser Weapons Technology III* (Vol. 4724, pp. 101-109). SPIE.

11. Glebov, A. L., Mokhun, O., Rapaport, A., Vergnole, S., Smirnov, V., & Glebov, L. B. (2012, May). Volume Bragg gratings as ultra-narrow and multiband optical filters. In *Micro-Optics 2012* (Vol. 8428, pp. 42-52). SPIE.

12. SeGall, M., Rotar, V., Lumeau, J., Mokhov, S., Zeldovich, B., & Glebov, L. B. (2012). Binary volume phase masks in photo-thermo-refractive glass. Optics letters, 37(7), 1190-1192.

13. Process for production of high efficiency volume diffractive elements in photo-thermo-refractive glass, US Patent 6586141 B1.

14. Glebov, Leonid. "Fluorinated silicate glass for conventional and holographic optical elements." Window and Dome Technologies and Materials X. Vol. 6545. International Society for Optics and Photonics, 2007.

15. Milam, D. (1998). Review and assessment of measured values of the nonlinear refractive-index coefficient of fused silica. Applied optics, 37(3), 546-550.

16. Glebov, L., Glebova, L., Rotari, E., Gusarov, A., & Berghmans, F. (2005, August). Radiation-induced absorption in a photo-thermo-refractive glass. In *Photonics for Space Environments X* (Vol. 5897, p. 58970J). International Society for Optics and Photonics.

17. Sidorov, A. I., Nikonorov, N. V., Ignatiev, A. I., & Nemilov, S. V. (2019). The effect of UV irradiation and thermal treatments on structural properties of silver-containing photo-thermo-refractive glasses: Studies by Raman spectroscopy. Optical Materials, 98, 109422.

18. Menczel, J. D., Judovits, L., Prime, R. B., Bair, H. E., Reading, M., & Swier, S. (2009). Differential scanning calorimetry (DSC). Thermal analysis of polymers: Fundamentals and applications, 7-239.

19. Deubener, J., Bornhöft, H., Reinsch, S., Müller, R., Lumeau, J., Glebova, L. N., & Glebov, L. B. (2009). Viscosity, relaxation and elastic properties of photo-thermo-refractive glass. Journal of Non-Crystalline Solids, 355(2), 126-131.

20. Stookey, S. D., Beall, G. H., & Pierson, J. E. (1978). Full-color photosensitive glass. Journal of Applied Physics, 49 (10), 5114-5123.

21. Cardinal, T., Efimov, O. M., Francois-Saint-Cyr, H. G., Glebov, L. B., Glebova, L. N., & Smirnov, V. I. (2003). Comparative study of photo-induced variations of X-ray diffraction and refractive index in photo-thermo-refractive glass. Journal of non-crystalline solids, 325(1-3), 275-281.

22. Efimov, O. M., Glebov, L. B., & Andre, H. P. (2002). Measurement of the induced refractive index in a photothermorefractive glass by a liquid-cell shearing interferometer. Applied Optics, 41 (10), 1864-1871.

23. V.A. Borgman, L.B. Glebov, N.V. Nikonorov, G.T. Petrovskii, V.V. Savvin, A.D. Tsvetkov. Photothermal refractive effect in silicate glasses. Sov. Phys. Dokl., 34, No 11 (1989) 1011-1013.

24. Glebov, L. (2008, October). Volume Bragg Gratings in PTR glass-New optical elements for laser design. In Frontiers in Optics (p. SThA4). Optica Publishing Group.

25. Lumeau, J., Glebova, L., Golubkov, V., Zanotto, E. D., & Glebov, L. B. (2009). Origin of crystallization-induced refractive index changes in photo-thermo-refractive glass. Optical materials, 32 (1), 139-146.

26. Glebov, L. B. (2004). Kinetics modeling in photosensitive glass. Optical Materials, 25(4), 413-418.

27. Glebov, L. B., Dokuchaev, V. G., Nikonorov, N. V., & Petrovskii, G. T. (1984, January). New effect of the interaction of optical radiation with glass. In Soviet Physics Doklady (Vol. 29, p. 57).

28. Glebov, L. B., Docuchaev, V. G., & Nikonorov, N. V. (1991). Glass matrix strain caused by photoinduced charging of point defects. Journal of non-crystalline solids, 128(2), 166-171.

29. Chamma, K., Lumeau, J., Glebova, L., & Glebov, L. B. (2010). Generation and bleaching of intrinsic color centers in photo-thermo-refractive glass matrix. Journal of non-crystalline solids, 356 (44-49), 2363-2368.

30. Glebov, L. B., & Glebova, L. (2004). Swelling of photo-thermo-refractive glass resulted from thermal development. Glass Science and Technology-Frankfurt Am Main-, 75, 294-297.

31. Cardinal, T., Efimov, O. M., Francois-Saint-Cyr, H. G., Glebov, L. B., Glebova, L. N., & Smirnov, V. I. (2003). Comparative study of photo-induced variations of X-ray diffraction and refractive index in photo-thermo-refractive glass. Journal of non-crystalline solids, 325(1-3), 275-281.

32. Glebov, L., Glebova, L., Tsechomskii, V., & Golubkov, V. (2004, September). Study of structural transformations in photo-thermo-refractive glass by SAXS and XRD. In Proceedings of XX International Congress on Glass.

33. S Lumeau, J., Glebova, L., Souza, G. P., Zanotto, E. D., & Glebov, L. B. (2008). Effect of cooling on the optical properties and crystallization of UV-exposed photo-thermo-refractive glass. Journal of non-crystalline solids, 354(42-44), 4730-4736.

34. J.H. Simmons, K.S. Potter, Optical Materials, Academic Press, 2000. pp. 153–154.

35. Julien Lumeau, Edgar Dutra Zanotto. A review of the photo-thermal mechanism and crystallization of photo-thermo-refractive (PTR) glass. International Materials Reviews, 2016; http://dx.doi.org/10.1080/09506608.2016.1264132 1-19.

36. Glebova, L., Klimov, M., Chamma, K., & Glebov, L. B. (2013, July). Photo-structural transformations in photo-thermo-refractive glass. In International Congress on Glass (Prague, Czech Republic), paper (Vol. 171).

37. Larissa Glebova, Helene Mingareev, Daniel Ott, Mikhail Klimov, Ivan Divliansky, Leonid Glebov. Effect of UV Exposure on Photoinduced Crystallization and Refractive Index Change in PTR Glass. 1st Joint meeting of DGG and ACerS GOMD; Session V.10 Glass Ceramics and Optical Ceramics; May 29, 2014 Aachen, Germany.

38. Glebova, L., Lumeau, J., Klimov, M., Zanotto, E. D., & Glebov, L. B. (2008). Role of bromine on the thermal and optical properties of photo-thermo-refractive glass. Journal of non-crystalline solids, 354(2-9), 456-461.

39. Shirshnev, P. S., Alvarez, R. A., & Glebov, L. B. (2021). Long-wavelength optical absorption edge of photo-thermo-refractive glass. Optical Materials Express, 11(9), 2883-2891.

40. Dotsenko, A. V., Glebov, L. B., & Tsekhomsky, V. A. (2020). Physics and chemistry of photochromic glasses. CRC Press.

41. Martins, M. A., Pinho, S. P., & Coutinho, J. A. (2019). Insights into the nature of eutectic and deep eutectic mixtures. Journal of Solution Chemistry, 48(7), 962-982.

42. Glebov, L. B. (2001, April). Optical absorption and ionization of silicate glasses. In Laser-Induced Damage in Optical Materials: 2000 (Vol. 4347, pp. 343-358). SPIE.

43. Glebov, L. B., & Boulos, E. N. (1998). Absorption of iron and water in the Na2O–CaO–MgO–SiO2 glasses. II. Selection of intrinsic, ferric, and ferrous spectra in the visible and UV regions. Journal of non-crystalline solids, 242(1), 49-62.

44. Glebova, L., Lumeau, J., & Glebov, L. B. (2011). Photo-thermo-refractive glass co-doped with Nd3+ as a new laser medium. *Optical Materials*, *33*(12), 1970-1974.

45. Weber, M. J. (1973). Optical spectra of Ce3+ and Ce3+-sensitized fluorescence in YAlO3. Journal of Applied Physics, 44 (7), 3205-3208.

46. Efimov, A. M., Ignat'ev, A. I., Nikonorov, N. V., & Postnikov, E. S. (2011). Spectral components that form UV absorption spectrum of Ce 3+ and Ce (IV) valence states in matrix of photothermorefractive glasses. Optics and Spectroscopy, 111 (3), 426.

47. Lixin Ning, Changbao Wu, Lanlan Li, Lihua Lin, Changkui Duan, Yongfan Zhang, and Luis Seijo "First-Principles Study on Structural Properties and 4f → 5d Transitions of Locally Charge-Compensated Ce3+ in CaF2", The Journal of Physical Chemistry C 2012 116 (34), 18419-18426.

48. Larissa Glebova, Doris Ehrt, Leonid Glebov. Luminescence of dopants in PTR glass. Phys. Chem. Glasses: Eur. J. Glass Sci. Technol. B, 48 (2007) 328–331.

49. Marie-Laure Brandily-Anne, Julien Lumeau, Larissa Glebova, Leonid B. Glebov. Specific absorption spectra of cerium in multicomponent silicate glasses. J. of Non-Crystalline Solids 356 (2010) 2337–2343.

50. Lumeau, J., Glebova, L., & Glebov, L. B. (2008). Influence of UV-exposure on the crystallization and optical properties of photo-thermo-refractive glass. Journal of non-crystalline solids, 354 (2-9) 425-430.

51. Lumeau L.B. Glebov. Glass Sci. Technol., 75 (C1) (2002), p. 73.

52. Kompan, F., Divliansky, I., Smirnov, V., & Glebov, L. B. (2018, February). Two-step recording of visible holographic elements in photo-thermo-refractive glass. In Components and Packaging for Laser Systems IV (Vol. 10513, pp. 155-166). SPIE.

53. Lumeau, J., Glebova, L., & Glebov, L. B. (2014). Absorption and scattering in photo-thermo-refractive glass induced by UV-exposure and thermal development. Optical Materials, 36(3), 621-627.

54. Chamma, K., Lumeau, J., Glebova, L., & Glebov, L. B. (2010, September). Effect of dosage and thermal treatment on photo-thermo-refractive glass crystallization properties. In International Congress on Glass (Salvador, Brazil), paper (Vol. 326).

55. Gy, R. (2008). Ion exchange for glass strengthening. Materials Science and Engineering: B, 149 (2), 159-165.

56. Kulp, A. B. (2012). Analysis of strength variation in glass due to ion exchange (Doctoral dissertation, Virginia Tech).

57. Glebov, L. B., Efimov, O. M., Nikonorov, N. V., & Petrovskiĭ, G. T. (1985). Optical breakdown of the surface of K8 glass modified by low-temperature ion exchange. Soviet Journal of Quantum Electronics, 15(10), 1410.

58. Lupascu, A. I., Kevorkian, A. P., Boudet, T., Saint-Andre, F., Persegol, D., & Levy, M. (1996). Modeling ion exchange in glass with concentration-dependent diffusion coefficients and mobilities. OptEn, 35, 1603-1610.

59. Aben, H., & Guillemet, C. (2012). Photoelasticity of glass. Springer Science & Business Media.

60. Tyagi, V., & Varshneya, A. K. (1998). Measurement of progressive stress buildup during ion exchange in alkali aluminosilicate glass. Journal of non-crystalline solids, 238(3), 186-192.

61. Brandenburg, A. (1986). Stress in ion-exchanged glass waveguides. Journal of lightwave technology, 4(10), 1580-1593.

62. Peters, P. M., Funk, D. S., Peskin, A. P., Veasey, D. L., Sanford, N. A., Houde-Walter, S. N., & Hayden, J. S. (1999). Ion-exchanged waveguide lasers in Er 3+/Yb 3+ codoped silicate glass. Applied optics, 38(33), 6879-6886.

63. Sgibnev, Y. M., Nikonorov, N. V., Vasilev, V. N., & Ignatiev, A. I. (2015). Optical gradient waveguides in photo-thermo-refractive glass formed by ion exchange method. Journal of Lightwave Technology, 33(17), 3730-3735.

64. White, J. M., & Heidrich, P. F. (1976). Optical waveguide refractive index profiles determined from measurement of mode indices: a simple analysis. Applied optics, 15(1), 151-155.

65. Ulrich, R., & Torge, R. (1973). Measurement of thin film parameters with a prism coupler. Applied Optics, 12(12), 2901-2908.

66. Glebov, L. B., Dokuchaev, V. G., & Morozova, L. S. (1989). A simple method for reconstruction of the refractive index profile of planar waveguides. Optics and Spectroscopy, 66, 649-651.